Deposited via The University of Sheffield.

White Rose Research Online URL for this paper:
https://eprints.whiterose.ac.uk/id/eprint/237712/

Version: Published Version

Dynamins maintain nuclear envelope homeostasis and genome stability

Célia Aveleira[1], Thibaud Martial [2], Loïc Carrique [3], Rita Gaspar[1], Ana Caulino-Rocha[1], Izaak Myatt[2], Franz Wendler[2], Pauline Lascaux [4], Misha Le Claire[3], James Bancroft[2], Carl Smythe[5], Kristijan Ramadan[4,6], Nuno Raimundo [1,7,8] & Ira Milosevic [1,2] ✉

The nuclear envelope is a protective barrier for the genome and a mechanotransduction interface between cytoplasm and nucleus, whose malfunction disrupts nucleocytoplasmic transport, compromises DNA repair, accelerates telomere shortening, and promotes genomic instability. Mechanisms governing nuclear envelope remodeling and maintenance in interphase and postmitotic cells remain poorly understood. Here, we report a role for dynamins, a family of essential brain-enriched membrane- and microtubule-binding GTPases, in preserving nuclear envelope and genomic homeostasis. Cells lacking dynamins exhibit nuclear envelope dysmorphisms, including buds with long narrow necks where damaged DNA frequently accumulates. These cells also show impaired autophagic clearance, reduced levels of key DNA repair proteins, and aberrant microtubules. Nocodazole treatment restores nuclear morphology and reduces DNA damage. Collectively, the data reveal that dynamins promote nuclear envelope homeostasis and removal of damaged DNA via their GTPase activity and interaction with microtubules, providing insights into mechanisms that uphold genome stability and counteract aging-related pathologies.

The nuclear envelope (NE) is a central organizing structure of eukaryotic cells, consisting of a double membrane, connected at specific points where the nuclear pores form, and an underlying nuclear lamina (yeast and many unicellular eukaryotes lack a discernible lamina). Lamins A, B, and C form the lamina, which provides mechanical strength and structural integrity support, and a spherical-like shape to the nucleus. In addition to nucleus integrity, the nuclear lamina has a role in chromatin organization, gene expression regulation, and cell division. Its perturbations and loss of NE homeostasis lead to decreased nucleocytoplasmic transport, faster telomere attrition, defective DNA damage repair and increased genomic instability[1–3], ultimately evolving into aging, cancer or (neuro)degenerative diseases[4,5]. NE undergoes dramatic changes during mitosis, yet less is known about the mechanisms underlying NE maintenance and their links to genome stability in interphase (the period of the cell cycle between cell divisions) and post-mitotic cells (e.g., neurons, cardiac myocytes).

Dynamin was first identified as a microtubule-binding protein[6–9]. Research efforts shifted to its role in membrane trafficking once functions for dynamin in receptor-mediated endocytosis and synaptic

[1]Multidisciplinary Institute of Aging, Centre for Innovative Biomedicine and Biotechnology, University of Coimbra, Coimbra, Portugal. [2]Centre for Human Genetics, Nuffield Department of Medicine, University of Oxford, Oxford, UK. [3]Division of Structural Biology (STRUBI), Centre for Human Genetics, Nuffield Department of Medicine, University of Oxford, Oxford, UK. [4]Department of Oncology, MRC Weatherall Institute of Molecular Medicine, John Radcliffe Hospital, University of Oxford, Oxford, UK. [5]School of Biosciences, University of Sheffield, Sheffield, UK. [6]Cancer Discovery and Regenerative Medicine Program, Lee Kong Chian School of Medicine, Nanyang Technological University, Singapore, Singapore. [7]Department of Cell and Biological Systems, Penn State College of Medicine, Hershey, PA, USA. [8]Penn State Cancer Institute, Hershey, PA, USA. ✉e-mail: Ira.Milosevic@well.ox.ac.uk

vesicle recycling were discovered[9–11]. To date, dynamin has been found to function in several cellular processes, most notably membrane fission during endocytosis[10,11], actin reorganization[11], centrosome cohesion[12], and dynamic instability of microtubules[13]. Three dynamin isoforms have been identified in vertebrates. Dynamin-1 and 3 are tissue-specific (brain for dynamin-1; brain, testis, lung, heart for dynamin-3), whereas dynamin-2 is ubiquitously expressed[14]. Dynamins have five characteristic domains: a GTPase domain that facilitates the conversion of guanosine triphosphate (GTP) to guanosine diphosphate (GDP); a γ-tubulin-binding middle domain; a membrane-interacting pleckstrin homology (PH) domain, a GTPase effector domain (GED), and a C-terminus proline-rich domain that binds to microtubules and various SH3 domain-containing proteins, like endophilins-A[15].

Three dynamin proteins are members of the dynamin superfamily that comprises a growing assortment of multi-domain GTPases with conserved propensity to self-assemble into oligomers[11]. Present from bacteria to humans, members of the dynamin superfamily participate in various membrane-remodeling events, as well as in whole-cell division (cytokinesis)[11,12]. While membrane remodeling appears to be a major feature, it is not the sole function of the dynamin superfamily: nearly all dynamin superfamily members display both membrane-dependent and membrane-independent roles. Namely, dynamin-related proteins can be recruited to the NE to facilitate membrane remodeling events essential for maintaining NE integrity - in unicellular ciliate *Tetrahymena thermophila*, the dynamin-related protein Drp6 is targeted to the nuclear membrane via interactions with specific lipids, and this interaction is crucial for nuclear expansion and macronucleus formation[16]. Additionally, yeast dynamin-like 1 (Dnm1) is involved in yeast nucleophagy, a process that removes nuclear and inner nuclear membrane cargo without compromising NE integrity[17].

Importantly, the NE shares structural similarities with other membrane systems, suggesting that proteins like dynamins, with a key role in membrane remodeling, could influence nuclear membrane dynamics. Here, we reveal new roles for dynamins 1, 2, and 3, best known for their function in endocytic vesicle fission and intracellular vesicle trafficking, in mediating NE homeostasis and DNA repair, shedding light on mechanisms that preserve genome stability and potentially protect against aging and aging-associated diseases[18].

Results

Loss of dynamins triggers nuclear envelope dysmorphisms

During our studies on dynamin-1,2,3 triple knock-out cells[19], we observed that cells without dynamins have abnormal nuclear appearance. Thus, we explored the role of membrane-binding dynamins in the homeostasis of the NE. Employing engineered mouse fibroblasts in which dynamins 1, 2, and 3 expression is blocked upon 4-hydroxytamoxifen (4-OHT) treatment[20] (henceforth dynamin-TKO; produced as detailed in Supplementary Fig. 1a, b; absence of dynamins is confirmed for each experiment as in Supplementary Fig. 1c), we examined the nuclear morphology by probing for DNA (Hoechst, SPY555-DNA™) and immunostaining against lamins-A/C (two key components of the nuclear lamina). DNA probes and lamin-immunostainings gave similar results with ~80% of dynamin-TKO cells presenting a prominent accumulation of nuclear dysmorphisms (lamins-A/C Fig. 1a–c; Hoechst Supplementary Fig. 2a, b). This includes the increased occurrence of invaginations, micronuclei (DNA-containing structures separated from the main nucleus) and blebs (Fig. 1d), reminiscent of similar phenotypes described in senescent cells, aged tissues and progeria models[4,21–25]. Notably, most nuclei showed a combination of dysmorphic phenotypes and were slightly larger (Supplementary Fig. 2c). The nuclear circularity index (perfect circle = 1) is decreased in dynamin-TKO cells (Fig. 1c and

Supplementary Fig. 2d), with roundness values reminiscent of progeria models and aged mammals[25–28]. Since some nuclear dysmorphisms were also observed in control (not 4-OHT-treated) cells, we performed the same experiments on wild-type (WT) mouse fibroblasts and noted no significant difference in the number of dysmorphic nuclei and circularity index between WT and dynamin-control cells (Fig. 1c). In addition, when WT fibroblasts were treated with 4-OHT (same concentration/duration as dynamin-TKO cells), no accumulation of nuclear dysmorphisms and no difference in the circularity index were observed (Supplementary Fig. 2e, f).

Interestingly, we also observed two additional distinct NE phenotypes in dynamin-TKO cells, which we referred to as nuclear buds (small structures connected to the NE usually through a long narrow neck; Fig. 1a, additional examples in Supplementary Fig. 2g) and lamin-A/C positive vesicles (small structures not connected to the nucleus, distinguished from micronuclei by their interphase origin, abundance and size; Fig. 1a and Supplementary Fig. 2h). These phenotypes occurred in ~16% and ~11% dynamin-TKO cells, respectively (Fig. 1e, f; $N > 2260$ cells/condition). Given that we did not observe these phenotypes in control cells, we reasoned that they were a direct consequence of dynamin absence, and focused further research on these features.

Notably, we also observed the presence of both NE-originating buds and vesicles in live cells, as detected by confocal microscopy in dynamin-TKO cells transiently expressing green fluorescent protein (GFP) fused to lamin-A (Supplementary Movie 1). To confirm that these phenotypes were specifically associated with dynamin, dynamin2-WT (the main dynamin in fibroblasts) was transiently reintroduced in dynamin-TKO cells, which was sufficient to rescue the nuclear size, shape and circularity (Fig. 1g, h and Supplementary Fig. 3a–c), despite small type-I invaginations could still be observed in some nuclei. However, expression of dynamin2-K44A, a dominant-negative mutant that lacks the GTPase activity[29], did not rescue the NE dysmorphisms in dynamin-TKO cells (Fig. 1g, h and Supplementary Fig. 3a–c). Also, no rescue of NE dysmorphisms in dynamin-TKO cells was observed upon expressing dynamin2-R361S-mRFP[30] or dynamin2-R399A-mRFP[30] mutants, which disrupt the tetrameric structure of dynamin in the unassembled state and impair its ability to stably bind to and nucleate higher-order self-assembly on membranes in these cells (Fig. 1i and Supplementary Fig. 3d). To further test if impaired dynamin function is sufficient to trigger nuclear phenotypes in WT cells, we transiently expressed dynamin2-K44A in WT cells, and observed more dysmorphic nuclei and decreased nuclear circularity (Fig. 1j, k). Lastly, we treated both human and mouse cells with the non-selective dynamin inhibitor dynasore[31], and observed a decrease in the NE circularity (Supplementary Fig. 4a–f; of note, dynasore may also have off-target effects[32,33]). Altogether, our results show that dynamins, and more specifically, dynamins' GTPase and assembly activities, are needed to maintain the NE homeostasis.

Dynamin deficiency decreases nuclear lamins, but does not compromise nuclear envelope integrity

Given that the nuclear shape and NE structure are maintained by lamins, we next tested if the loss of dynamins impacts the levels of these proteins. We observed that all three lamins (A, B, and C) were down-regulated in dynamin-TKO cells (Fig. 2a, b), as also detected in various pathologies and aged cells[23,25,34,35]. To determine the reason behind the down-regulation of lamin-A/C expression, we first ruled out the effects of 4-OHT itself (Supplementary Fig. 5a), and subsequently found that transcript levels of *Lmna* gene were not altered (Fig. 2c), but the proteosomal degradation contributed to lower protein levels of lamin-A and lamin-C (Fig. 2d). Since the decrease of lamins may affect the NE integrity, we next examined the integrity of NE in control and dynamin-TKO cells by a well-established probe encoding NLS-mCherry[32]. We observed no significant presence of red fluorescence

2
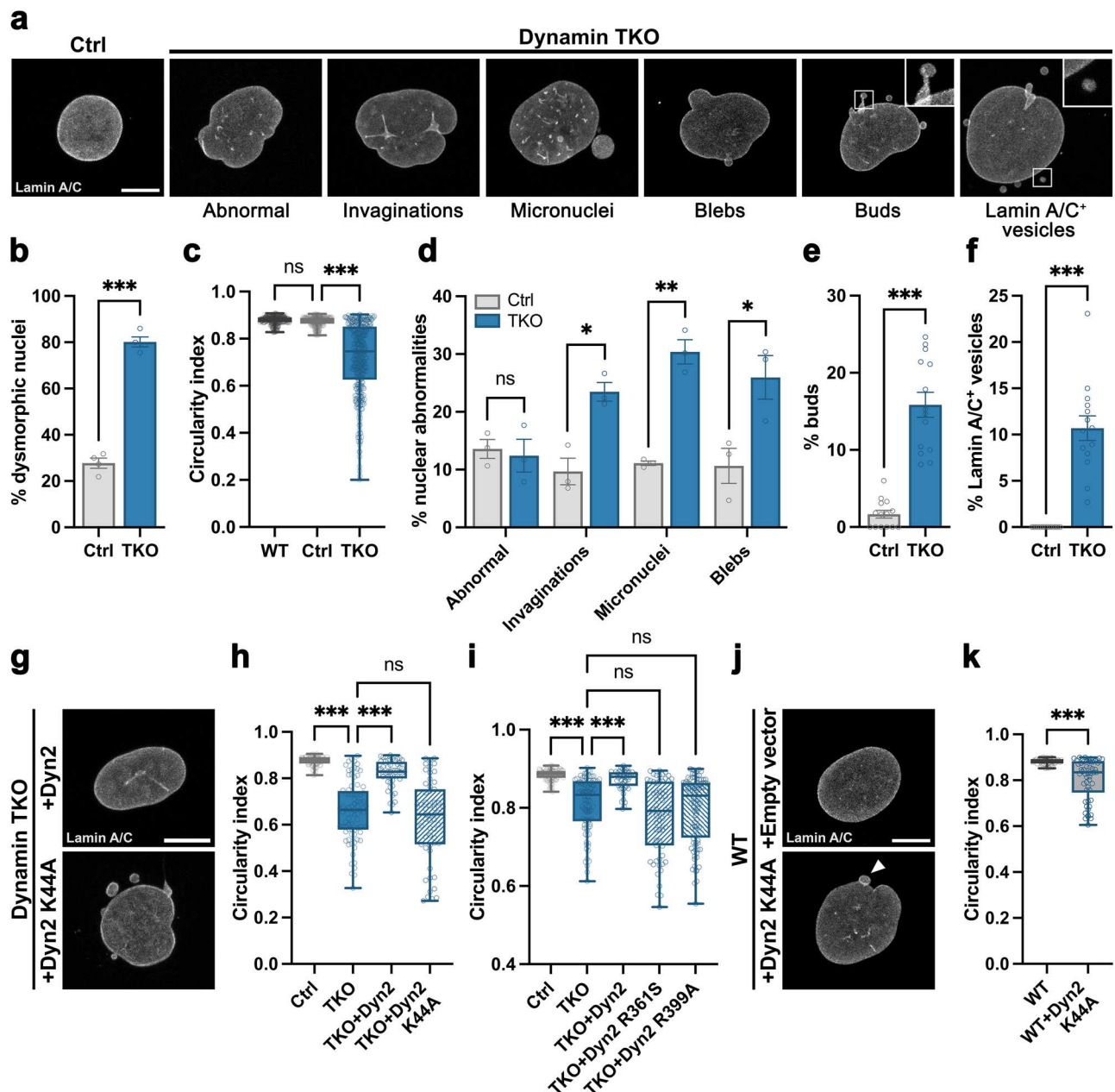
Fig. 1 | Dynamin deficiency results in nuclear envelope (NE) dysmorphisms.
a Representative images of lamin A/C immunostained nuclei in control and dynamin TKO cells. Scale bar 10 μm; insets 5.4 μm. Quantification of dysmorphic nuclei (**b**), and circularity (**c**) in wild-type, control and dynamin TKO cells. Four (**b**) and five (**c**) independent biological replicates; >317 cells/condition. Quantification of types of nuclear abnormalities (**d**), buds (**e**) and lamin A/C-positive vesicles (**f**) in control and dynamin TKO cells. Three (**d**) and fourteen (**e**, **f**) independent biological replicates; >2250 cells/condition. Representative images of lamin A/C immunostained nuclei in dynamin TKO cells transfected with dynamin2-WT (top; (**g**)) or dynamin2-K44A mutant for 24 h (bottom; (**g**)), and respective quantification of nuclear circularity (**h**). Scale bar 10 μm. Four independent biological replicates; >52 cells/condition. **i** Quantification of nuclear circularity of dynamin2-R361S and dynamin2-R399A mutants expressed for 24 h in dynamin-TKO cells, compared to control, TKO and TKO with dynamin-2. Three independent biological replicates; >49 cells/condition. This experiment was performed independently of experiments shown in (**h**), using another microscopy system. **j, k** Representative images of nuclei in wild-type mouse fibroblasts 24 h after transfection with pEGFP vector as control (top; (**j**)) or dynamin2-K44A mutant (bottom; (**i**)), and respective quantification of nuclear circularity (j). Scale bar 10 μm. Three independent biological replicates; >53 cells/condition. Data are presented as bar charts with mean ± standard error of the mean (SEM), and as box plots showing the 25th percentile (Q1), median, 75th percentile (Q3), and whiskers extending to the minimum and maximum values. Statistical significance is indicated as ns, not significant; *$p < 0.05$; **$p < 0.01$; ***$p < 0.001$. Statistical analyses were performed using two-tailed unpaired Student's t test with Welch's correction (**b**: $p < 0.0001$, **d**: abnormal: 0.7424, invaginations $p = 0.0107$, micronuclei $p = 0.0098$, blebs $p = 0.0366$, two-tailed Mann–Whitney U-test (**e**: $p < 0.0001$, **f**: $p < 0.0001$, **k**: $p < 0.0001$), and one-way ANOVA Kruskal–Wallis test followed by post-hoc Dunn's multiple comparisons test (**c**: $p = 0.1885$, $p < 0.0001$, **h**: $p < 0.0001$, $p < 0.0001$, $p > 0.9999$, **i**: $p < 0.0001$, $p < 0.0001$, $p > 0.9999$, $p > 0.9999$). Ctrl Control, TKO Triple knockout, WT Wild-type.

in the cytosol of either control or dynamin-TKO cells (Fig. 2e). Comparable numbers of cells with ruptured nuclei occurred in both control and dynamin-TKO cells (Fig. 2f). To characterize the appearance of the outer nuclear membrane (ONM) and determine whether the NE abnormalities in dynamin-TKO cells are also revealed by this probe,

we expressed a fluorescently tagged version of the ONM protein nesprin-3 in both control and dynamin-TKO cells. Nesprin-3 localized to the ONM as expected (Fig. 2g). Notably, it also labeled emerging NE buds and lamin A/C-positive vesicles in dynamin-TKO cells (Fig. 2g).
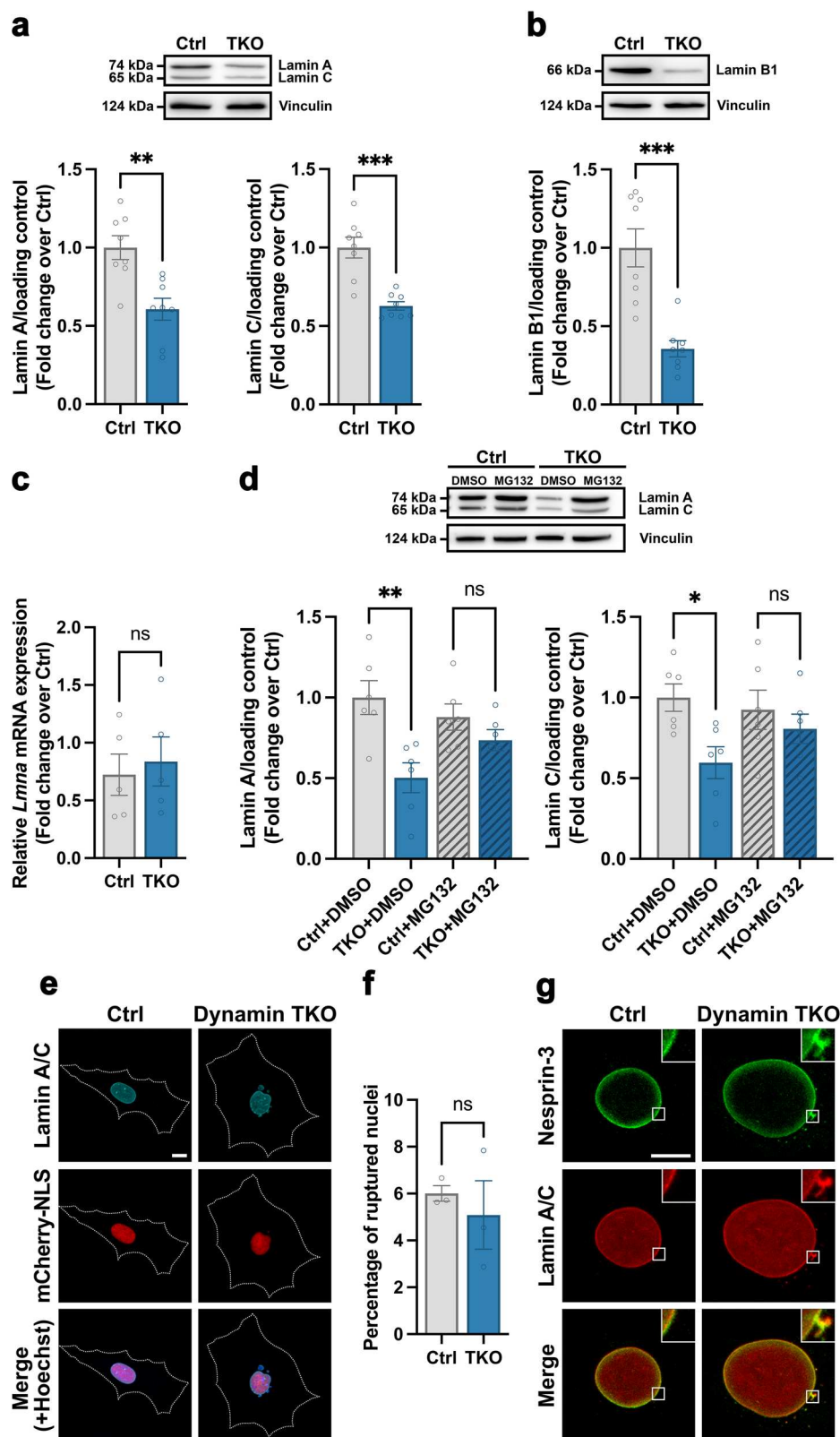
Dynamin TKO cells do not show significant cell death

We next examined if the NE buds and lamin-A/C positive vesicles could be a consequence of early cell death in dynamin-TKO cells. We assessed cell viability and apoptosis rates in control and dynamin-TKO cells by several approaches, namely trypan blue exclusion assay (Fig. 3a), immunocytochemistry against cleaved caspase-3 (Fig. 3b, c), propidium iodine/annexin-V assay (Fig. 3d), and TUNEL assay (Fig. 3e, f). No increased levels of cell death were observed in any of these assays in dynamin-TKO cells (Fig. 3a–f).

Dynamin is detected in the nuclear fraction and transiently interacts with the nuclear envelope

Next, we inspected if membrane-bound dynamins can be detected at the NE. We first isolated nuclei by subcellular fractionation, and

Fig. 2 | Dynamin deficiency decreases nuclear lamins in dynamin TKO cells but does not affect nuclear envelope integrity. a Western blot of lamins A and C (top) and respective quantifications (bottom). Vinculin was used as a loading control. Eight samples/condition. **b** Western blot of Lamin B1 (top) and respective quantification (bottom). Vinculin was used as a loading control. Eight samples/condition. **c** RT-qPCR of Lmna in control and dynamin TKO cells. Five independent biological replicates. **d** Western blot of lamins A and C (top) and respective quantifications (bottom) upon proteasomal inhibition with MG132. Vinculin was used as a loading control. Six samples/condition. **e, f** Representative stacked confocal images of control and dynamin TKO cells transfected with NLS-mCherry for 24 h and stained with anti-lamin A/C antibody. Note that cell fluorescence is localized to the cell nucleus (**e**) and respective quantification of cells with ruptured nucleus (**f**). Scale bar 10 μm. Three independent biological replicates. **g** Representative images of Emerald-nesprin 3 expressed in control and dynamin TKO cells for 24 h and stained with anti-lamin A/C antibody. Scale bar 10 μm. Data are presented as bar charts with mean ± SEM, ns, not significant; *$p < 0.05$; **$p < 0.01$; ***$p < 0.001$. Statistical analyses were performed using two-tailed unpaired Student's t test with Welch's correction (**a**: lamin A: $p = 0.0020$, lamin C: $p = 0.0005$, **b**: $p = 0.0007$, **c**: $p = 0.6911$, **d**: lamin A: $p = 0.0054$, $p = 0.2008$, lamin C: $p = 0.0114$, $p = 0.4560$, **f**: $p = 0.5967$). Ctrl Control, TKO Triple knockout, WT Wild-type.

detected dynamins (using a pan-dynamin antibody capable of detecting all three dynamins) in the nuclear fraction of WT mouse fibroblasts (Fig. 3g). We then inspected for possible accumulations of dynamin signal at the NE by live confocal imaging. Given that the NE buds with long, narrow necks were not detected in the WT cells (presumably the process becomes rate-limiting only in the absence of dynamins), we expressed the non-hydrolytic dynamin2-K44A-mRFP mutant in dynamin-TKO cells, and observed accumulations of this dynamin mutant in the nuclear proximity in live dynamin-TKO cells (Fig. 3h, with insets detailing dynamin signal at the nuclear bud). Similarly, a persistent (longer than a few minutes) accumulation of dynamin2-K44A-RFP was detected in the nuclear proximity (determined by GFP-lamin-A signal) in live control cells (Supplementary Fig. 5b). When dynamin2-WT is reintroduced in dynamin-TKO cells, NE buds were no longer enriched, and dynamic dynamin2-WT fluorescent punctate signal was occasionally detected at the nuclear surface (Supplementary Fig. 5c). Live accumulation of dynamin2-K44A at NE buds together with rescue by dynamin2-WT supports the interpretation of necked vesicles as remodeling intermediates. Altogether, dynamin was found in the nuclear fraction and transiently at the NE in live mammalian cells.

Ultrastructural analysis of dynamin-TKO cells reveals stalled vesicles with long, narrow necks

To examine the NE appearance in dynamin-TKO cells at the ultrastructural level, we used bi-color cryo-fluorescence combined with focused-ion beam milling and cryo-electron tomography (cryo-ET), a label-free cryogenic imaging pipeline that provides 3D datasets of organelles at nanometer resolution in their physiological environment[36]. For these experiments, dynamin-TKO cells stably expressing GFP-lamin-A through lentiviral integration and co-stained with SPY555-DNA™ were grown on gold carbon-coated grids and vitrified through plunge freezing. Approximately 200 nm thick, electron-transparent lamellae of frozen hydrated cells were generated for further analysis by cryo-ET. The lamella placement was first guided by the fluorescence signals in two channels (Supplementary Fig. 6a), then excess of cellular material was progressively milled away using an Argon plasma beam (Supplementary Fig. 6b). A final fluorescent stack was acquired on the lamella (Supplementary Fig. 6c) before transfer and acquisition of cryo-ET data (Supplementary Fig. 6d). Several tilt-series were collected along the NE in nuclear proximity. We observed distinct, recurrent morphologies in dynamin-TKO samples that were not observed in the control cells: (i) prominent "blisters" of the ONM (like the ones we reported in ref. 37; Fig. 4a), (ii) vesicle-like structures delimited by ONM, connected to the NE lumen by a long narrow membrane neck (enlarged in inset), consistent with impaired fission or altered budding dynamics (Fig. 4b), (iii) irregular vesicle-like structures delimited by ONM connected to cytoskeleton (arrowhead) and the NE lumen by a long narrow membrane neck (enlarged in inset) (Fig. 4c). In addition, double membrane vesicle-like structures that contain DNA in it were also detected (Fig. 4d, see another example in Fig. 4a). We used MemBrain software to perform automatic segmentation of the reconstructed tomograms, as shown in Fig. 4a'–d', and overlaid the segmented structures with original reconstruction (Fig. 4a"–d"). Based

on the lamin-A fluorescent signals, we expected to see double membrane structures, or buds filled with other vesicles, originating from the INM[38], yet, unexpectedly, those structures were not detected. We collected 38 tomograms in total, among which 7 showed the ONM forming buds with a narrow neck. We measured the size of the neck at different distances from the ONM: the width ranged from 7.7 nm to 24 nm. Of note, decreased levels of lamins, as in dynamin-TKO cells, can lead to the loss of INM integrity[39–41]. Hence, the majority of observed lamin-A positive structures may lack a detectable INM but contain a reminiscent lamin mesh, given that lamins interact with chromatin/DNA[42]. The observed NE phenotypes are consistent with the idea that fission of vesicle-like structures from the ONM gets stalled, or delayed, in the absence of dynamin (as also seen at the plasma membrane[11,20]), i.e., that dynamins promote fission from the ONM. Alternatively, these structures are formed at a higher rate in the absence of dynamins.

Dynamin deficiency triggers DNA damage accumulation

To investigate if the accumulation of NE-originating buds/vesicles affects genome maintenance, we examined the level of DNA damage in dynamin-TKO cells, and monitored if these structures contain damaged DNA. Abundant accumulation of phosphorylated histone 2AX (γ-H2AX), a well-established DNA damage marker[43], was observed in dynamin-TKO cells compared to control cells (Fig. 5a, b). Of note, WT cells treated with 4-OHT did not have notable increase in nuclear γ-H2AX signal (by immunocytochemistry, Supplementary Fig. 7a, b; Western blotting, Supplementary Fig. 7c). Notably, most, but not all (Fig. 5a, arrowhead), lamin-A/C-positive buds and vesicles contained detectable γ-H2AX signal in dynamin-TKO cells (Fig. 5a, enlarged views on the right). Further, we confirmed the increase in H2AX phosphorylation in dynamin-TKO samples in whole cell extracts by Western blotting (Fig. 5c). To test if DNA damage also accumulates in live cells, we transfected control and dynamin-TKO cells with lamin-A-mRFP and with EGFP-53BP1. This protein colocalizes with DNA double-strand breaks (DSB), the most deleterious DNA lesions[44]. We noted that the 53BP1 signal gets enriched in the proximity of most buds and in their lumen (Fig. 5d), in support of the idea that the NE structures abundantly seen in dynamin-TKO cells may serve to export damaged DNA and proteins from the nucleus.

To assess directly the level of DNA damage in dynamin-TKO cells, we used Comet assay under alkaline conditions[45]. The alkaline comet assay was used to examine both single-stranded and double-stranded DNA breaks (Supplementary Fig. 8a, b). We observed an increase in the Olive tail moment in dynamin-TKO cells, which is consistent with an increase in damaged DNA (Fig. 5e, f and Supplementary Fig. 8c–h).

We next tested if the re-expression of dynamin2-WT in dynamin-TKO cells can rescue DNA damage accumulation, given that it is able to rescue nuclear dysmorphisms. Notably, expression of dynamin2-WT-GFP in dynamin-TKO cells diminished the γ-H2AX signal, whereas expression of the dynamin2-K44A-GFP mutant did not (Fig. 5g, h). Next, we expressed dynamin2-K44A-GFP in WT cells and observed a strong increase γ-H2AX signal (Fig. 5i, j), revealing that dynamin's GTPase activity is needed for DNA homeostasis. We further pharmacologically inhibited dynamin in the WT cells (as above, using non-
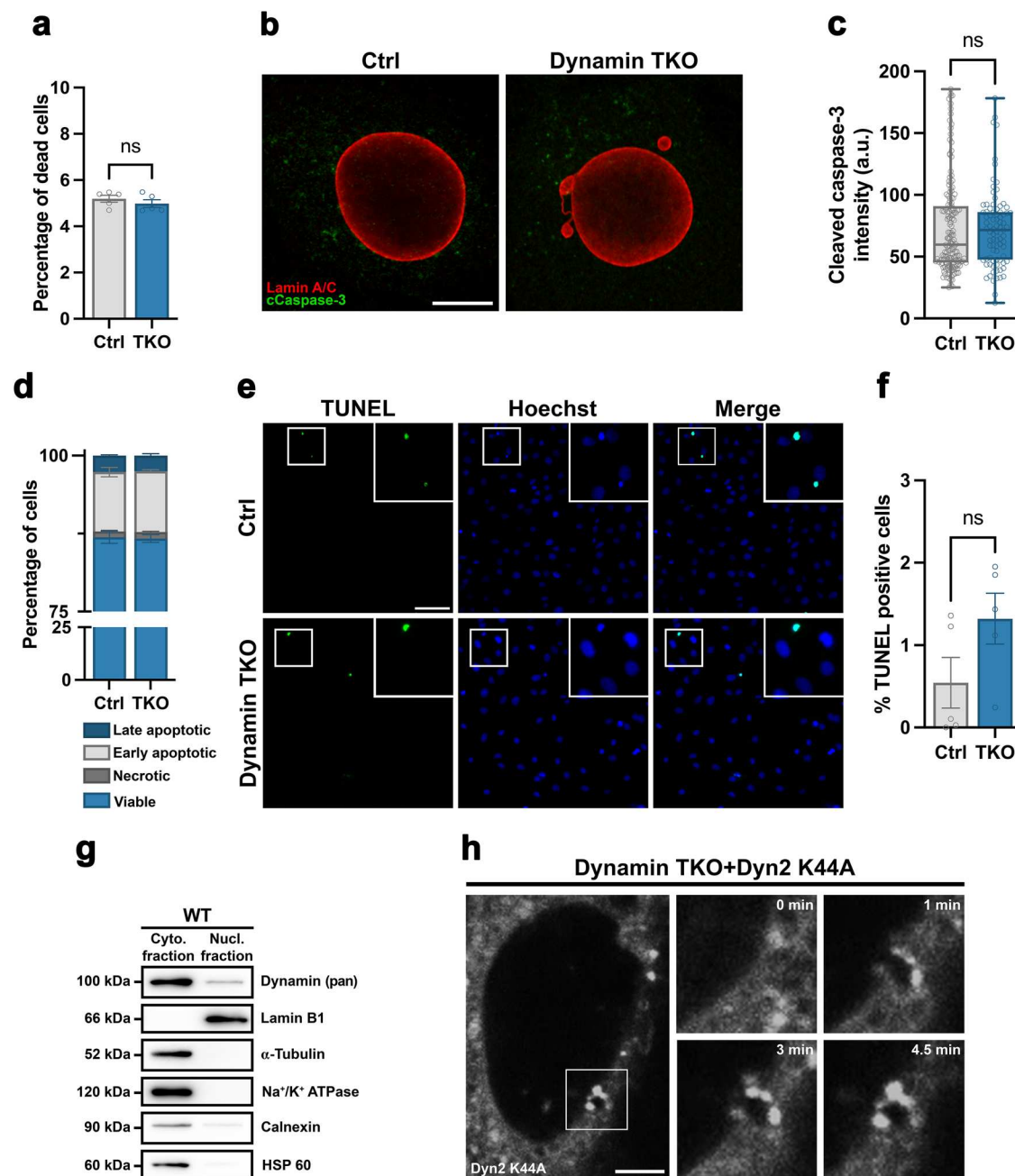
Fig. 3 | Dynamin is present in the nuclear fraction, and its ablation does not cause cell death. a–f Cell viability and apoptosis assays in dynamin-TKO cells compared to ctrl cells. **a** Percentage of dead cells after trypan blue application in cultured control and dynamin TKO cells. Five independent biological replicates. Representative images of lamin A/C and cleaved caspase-3 immunostained nuclei in control and dynamin TKO cells (**b**), and respective quantification of cleaved caspase-3 signal (**c**). Scale bar 10 μm. Three independent biological replicates; >85 cells/condition. **d** Percentage of viable/healthy (Annexin V−/PI−), necrotic (Annexin V−/PI+), early apoptotic (Annexin V+/PI−), and late apoptotic (Annexin V+/PI+) cells in control and dynamin TKO cells. Representative plots showed ~4% cells in the control group were dead or undergoing apoptosis, a usual level for cells growing in cultures. Three independent biological replicates. **e, f** Representative images of DAPI stained control and dynamin TKO cells after TUNEL assay (**e**), and respective quantification of TUNEL positive cells. Scale bar

100 μm; insets 100 μm. Five independent biological replicates. **g** Western blots after subcellular fractionation of wild-type cells into nuclear and cytoplasmic fractions. Five independent biological replicates. **h** Live-cell imaging of dynamin2-K44A-mRFP mutant expressed in dynamin TKO cells for 24 h by spinning-disk microscopy (red channel; optical cross-section through the cell is shown). Insets detail dynamin2-K44A enrichment at the nuclear bud (determined by negative staining) in live dynamin TKO cells. Scale bar 5 μm; insets 7 μm. Data are presented as bar charts with mean ± SEM, and as box plots showing the 25th percentile (Q1), median, 75th percentile (Q3), and whiskers extending to the minimum and maximum values; statistical significance is indicated as ns, not significant. Statistical analyses were performed using two-tailed unpaired Student's t test with Welch's correction (**a**: $p = 0.3881$, **d**: viable: $p = 0.7690$) and two-tailed Mann–Whitney U-test (**c**: $p = 0.5041$, **f**: $p = 0.0952$). a.u. Arbitrary units, Ctrl Control, TKO Triple knockout.

selective dynasore) and noted an increase in γ-H2AX signal (Supplementary Fig. 9a, b). The increased levels of γ-H2AX were also detected in human cells treated with a dynamin inhibitor (Fig. 5k, i), showing that this phenotype is not species-specific.

Decreased levels of key DNA damage repair proteins in dynamin-TKO cells

To determine if the accumulation of DNA damage detected by γ-H2AX and 53BP1 signals in dynamin-TKO cells may arise from
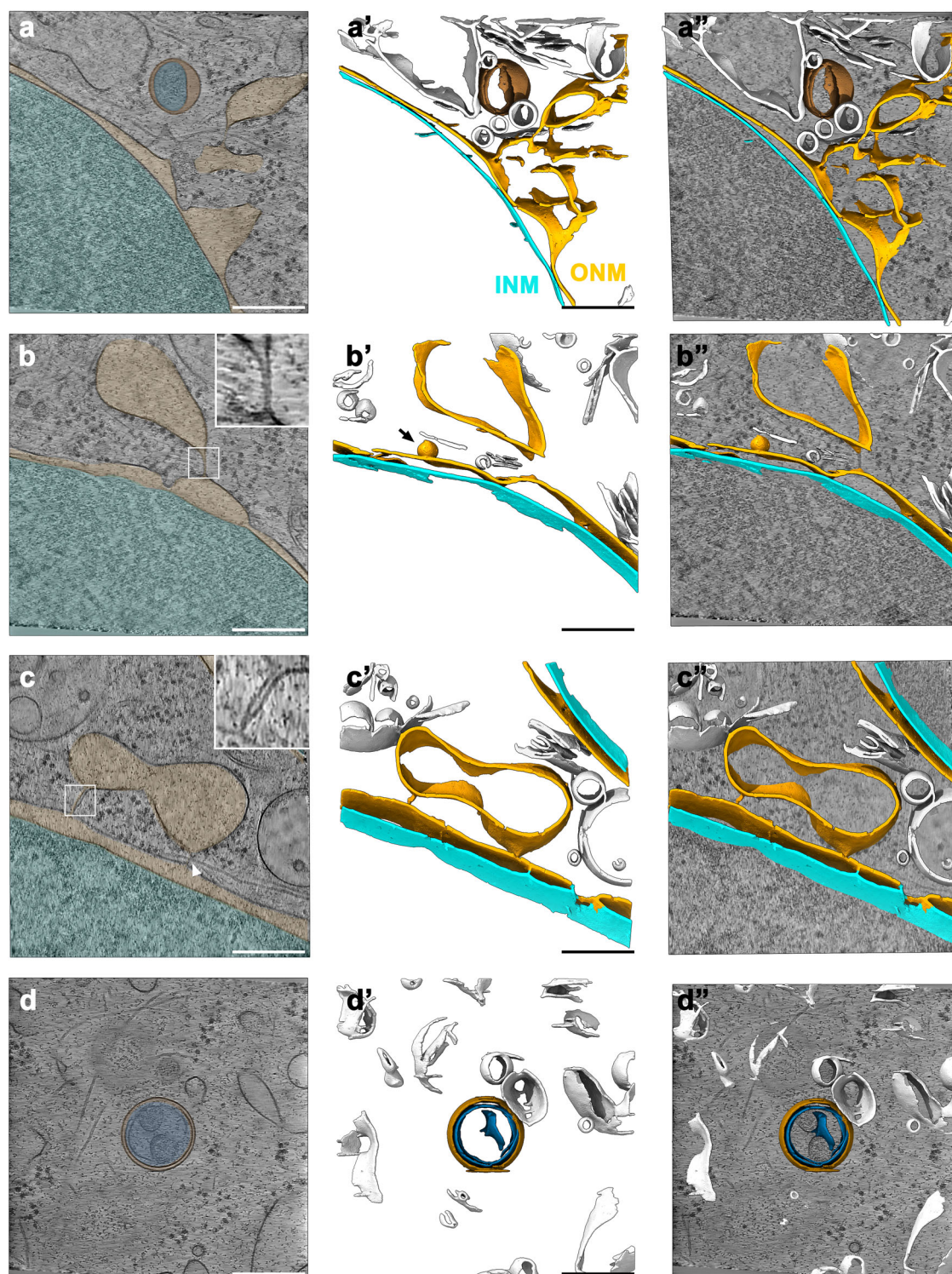
Fig. 4 | Ultrastructural analysis of nuclear envelope in dynamin TKO cells.
a−**d** Representative tomograms (left) of dynamin TKO cells, computational three-dimensional reconstruction (middle), and merge of the computational rendering over the tomogram (right). **a**−**a"** "Budding" of the outer nuclear membrane (ONM). **b**−**b"** Vesicle-like structures delimited by ONM, connected to the NE lumen by a long narrow membrane neck (inset) as if undergoing fission. Of note, these structures present ribosomes on their surface suggesting a link between NE remodeling and the ER. The size of small bud seen on the computational three-dimensional reconstruction is 70 nm (arrow).

c−**c"** Irregular vesicle-like structure delimited by ONM, connected to the cytoskeleton (arrowhead) and the NE lumen by a long narrow membrane neck (inset). **d**−**d"** Double membrane vesicle-like structure containing DNA. Scale bar 300 nm; insets 205 nm. MemBrain software was used for automatic segmentation of reconstructed tomograms. Color code: yellow−outer nuclear membrane (ONM), cyan−inner nuclear membrane (INM); brown/blue−small vesicles with DNA/nuclear material present in their lumen; white−segmented membranes in the nuclear proximity with no connection to the NE (see "Methods" for the classification criteria).
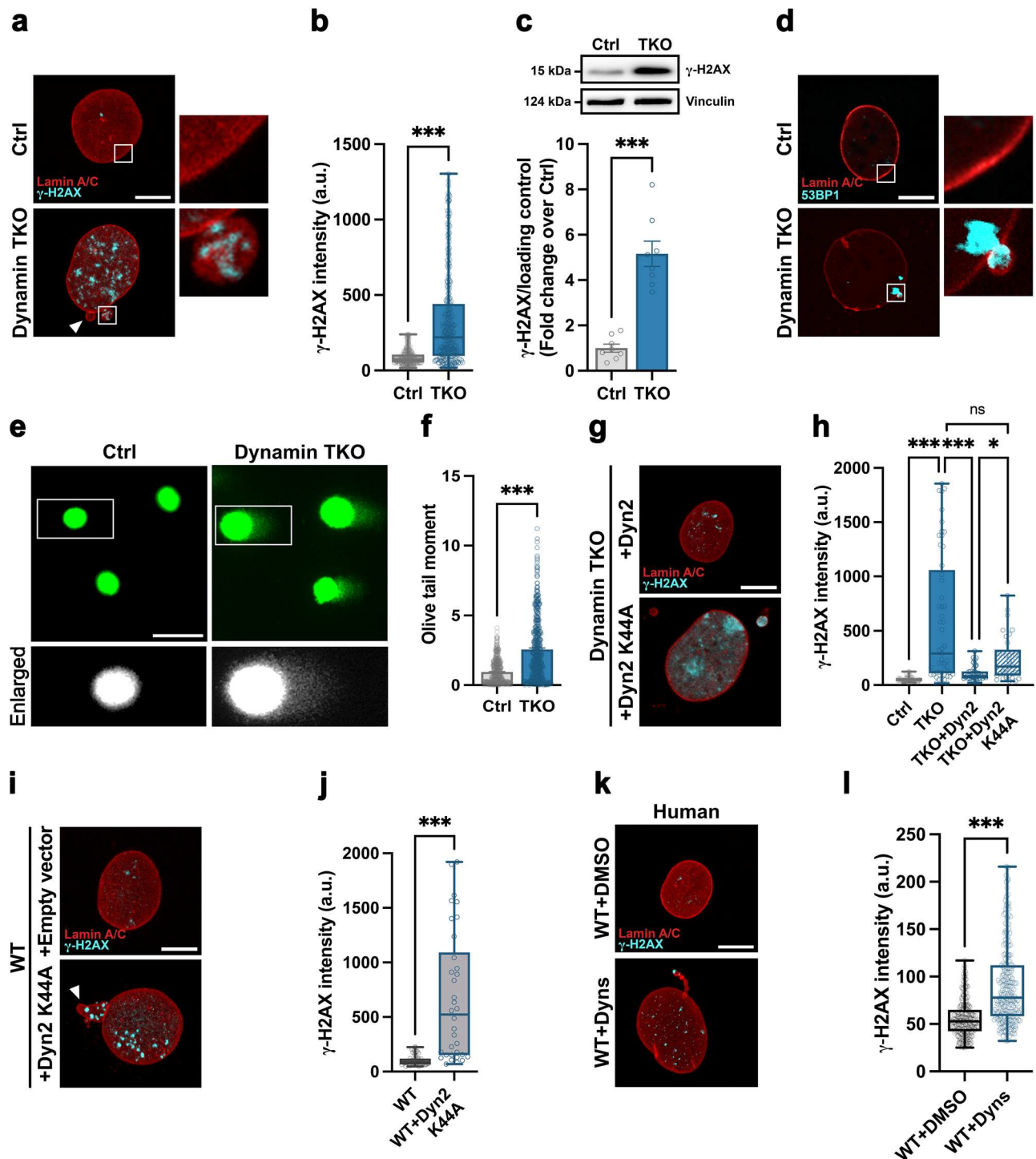
deficient DNA repair, we measured the activation of several proteins involved in the DNA damage response. The levels of p53, p21, proliferating cell nuclear antigen (PCNA), ATM (serine 1981) phosphorylation, and RAD51[46,47], were found to be down-regulated in dynamin-TKO samples (Fig. 6a–d, g). In addition, the nuclear levels of both activated ATM (phosphorylated ATM)(Fig. 6e, f) and RAD51 (Fig. 6h, i) were found to be decreased in dynamin-TKO cells. Of note, introduction of dynamin2-K44A mutant did not rescue nuclear RAD51 intensity, implying that the DNA repair capacity may be compromised in the presence of dynamin2-K44A (Supplementary Fig. 9c). These results suggest a decrease in the capacity of DNA repair in the absence of dynamins that may contribute to an accumulation of DNA damage, in addition to the roles of dynamin in promoting removal of

damaged DNA from the nucleus. These data are in agreement with a study of cancer cells where downregulation of dynamin expression was linked to deficient DNA repair[48].

We next explored how dynamin-TKO cells, which accumulate DNA damage and NE dysmorphisms, respond to a condition that induces (additional) DNA damage. Most therapies for advanced cancers are based on the use of chemotherapeutics, such as camptothecin (CPT)[49,50]. It has been recently shown that DNA damage induced by CPT can be processed by selective autophagy[37]. CPT induces topoisomerase-1 cleavage complexes (TOP1cc) DNA damage, and subsequent transient NE blebbing in human cells[37]. When dynamin-TKO cells were treated with CPT for 30 min, we observed increased levels of DNA damage and a nearly two-fold increase in the number of

Fig. 5 | Absence of dynamin leads to accumulation of DNA damage. Representative images of lamin A/C and γ-H2AX immunostained nuclei in control and dynamin TKO cells (**a**), and respective quantification of γ-H2AX signal per nuclear area (**b**). Scale bar 10 μm; insets 5 μm. Four independent biological replicates; >304 cells/condition. **c** Western blot of γ-H2AX (top) and respective quantification (bottom). Vinculin was used as a loading control. Eight biological samples/condition. **d** Representative images of live control and dynamin TKO cells transiently expressing lamin A-mRFP and EGFP-53BP1, imaged by the spinning-disk confocal microscope. A single optical section is shown, at difference to other figure panels with lamin and γ-H2AX, which were acquired by confocal microscopy and show maximal projections. Scale bar 10 μm; insets 5 μm. Three independent experiments. Representative images of control and dynamin TKO cells analysed by alkaline comet assay (**e**), and respective quantification of DNA damage (**f**; Olive tail moment = [tail mean-head mean] x % of DNA in the tail). Scale bar 50 μm; insets 90 μm. Three biological replicates, >465 cells/condition. Representative images of lamin A/C and γ-H2AX immunostained nuclei in dynamin TKO cells after transfection with dynamin2-WT or dynamin2-K44A (**g**), and respective quantification of γ-H2AX signal (**h**). Scale bar 10 μm. Three biological replicates; >34 cells/condition. **i, j** Representative images of wild-type cells after transfection with pEGFP vector as control (top) or dynamin2-K44A (bottom) and immunostained against lamin A/C and γ-H2AX (**i**), and respective quantification of γ-H2AX signal. Scale bar 10 μm. Three biological replicates, >34 cells/condition. **k, l** Representative images of lamin A/C and γ-H2AX immunostained nuclei in wild-type human fibroblasts treated with DMSO (control) or non-selective dynamin inhibitor dynasore (**c**), and respective quantification of γ-H2AX signal (**d**). Scale bar 10 μm. Three independent biological replicates, >225 cells/condition. Data are presented as bar charts with mean ± SEM, and as box plots showing the 25th percentile (Q1), median, 75th percentile (Q3), and whiskers extending to the minimum and maximum values; statistical significance is indicated as ns, not significant; *$p < 0.05$; ***$p < 0.001$. Statistical analyses were performed using two-tailed Mann–Whitney U-test (**b**: $p < 0.0001$, **f**: $p < 0.0001$, **j**: $p < 0.0001$, **l**: $p < 0.0001$), two-tailed unpaired Student's t test with Welch's correction (**c**: $p < 0.0001$), and one-way ANOVA Kruskal–Wallis test followed by post-hoc Dunn's multiple comparisons test (**h**: $p < 0.0001$, $p < 0.0001$, $p = 0.0465$, $p > 0.9999$, respectively). a.u. Arbitrary units, Ctrl Control, TKO Triple knockout, WT Wild-type.

NE buds/cell (Supplementary Fig. 9d). Given that repair of TOP1cc depends on their exit out of the nucleus[37], we propose that dynamins may play a role in the selective autophagy in DNA damage repair that protects genome stability as described in ref. 37, and it may be clinically relevant for cancer treatments and other diseases where advanced age may be a risk factor. This hypothesis is additionally supported by similar ultrastructural phenotypes, especially those shown in Fig. 4a, detected by cryo-ET.

Dynamin-TKO cells accumulate autophagosomes

We observed that dynamin-TKO cells show accumulation of DNA damage combined with a reduction in levels of several proteins involved in DNA repair. These observations are consistent with the view that, in the absence of dynamins, there might be a generalized failure of nuclear-selective autophagy. Dynamin-2 is reported to have a role in maturation of an autophagic compartment[33]. To examine autophagy and its flux in control and dynamin-TKO cells, we first inspected levels of LC3B-II and found them to be significantly increased (Fig. 7a), suggesting that there is no defect in autophagosome formation and that autophagosomes are accumulating. To confirm these results, we expressed LC3B-mRFP in control and dynamin-TKO cells, and observed robust accumulation of autophagosomes and an increase in their sizes (Fig. 7b, c). This suggests a lower autophagic flux, which is corroborated by increased levels of autophagy adapter protein p62/SQSTM1 that binds autophagy cargo (Fig. 7d) and direct measurements of autophagic flux (Fig. 7e, f). The lower autophagic flux is not due to a decrease in lysosomal mass, as the levels of lysosomal protein LAMP1 were found to be increased in dynamin-TKO cells (Fig. 7g). These data suggest that dynamin-TKO cells can form autophagosomes, however we cannot exclude the possibility that lysosomes are less functional in these cells, which may relate to compromised DNA damage clearance in the whole cell extracts.

Nocodazole treatment rescues nuclear envelope dysmorphisms and restores DNA homeostasis in dynamin-TKO cells

Besides their role in membrane fission, dynamins are known for their direct interaction with microtubules[6,9,13], which stimulates dynamin's GTPase activity. Microtubules are both dynamic structural elements and tracks for intracellular transport[51], and are known to play a key role in DNA repair[52,53]. Hence, we tested if microtubules and, specifically, tubulin acetylation, which regulates microtubule dynamics and stability, were altered in dynamin-TKO cells. We noted a robust increase in acetylated tubulin (Fig. 8a; notably, increased tubulin acetylation was also observed when only dynamin-2 protein is knocked-down[13]) and changes in the perinuclear tubulin morphology in dynamin-TKO cells (Fig. 8b). To test if these findings may be linked to the NE phenotypes,

we treated dynamin-TKO cells with nocodazole, a drug that interferes with the polymerization of microtubules and disrupts their dynamics[54,55], and observed that this treatment was sufficient to restore the nuclear circularity (Fig. 8c, d) and size (Fig. 8e). Interestingly, nocodazole treatment also decreased the levels of DNA damage in dynamin-TKO cells (Fig. 8c, f). We verified this unexpected rescue independently by an alkaline Comet assay, and observed no significant difference in Olive tail moments between control and nocodazole-treated dynamin-TKO cells (Fig. 8g, h and Supplementary Fig. 9e–g), indicating a correction of DNA damage. While these findings raise exciting questions, including in the context of microtubules promoting dynamin's GTPase activity[7], further work is needed to elucidate how dynamin-microtubule interactions maintain NE and genome stability. Based on our data, it is possible that mammalian dynamins play a role in membrane fission at the ONM, and/or hamper intracellular transport and DNA damage repair factors translocation to the nucleus, among other possible mechanisms.

Discussion

Dynamin-TKO cells reveal the presence of a membrane fission pathway in mammalian cells in which NE components, including lamins, may be isolated away from the bulk of the nuclear compartment. This process appears to operate to maintain NE homeostasis, as in the absence of dynamins, cell nuclei develop dysmorphic structures. The NE buds and vesicles contain both nesprin-3, an ONM protein, as well as A/C-type lamins, which are the innermost components of the NE, suggesting that fission involves the vesiculation of the NE. Taken together, our data suggest that the absence of dynamins results in a delay in this fission pathway, causing the build-up of additional membrane, resulting in misshapen nuclei.

NE buds with long, narrow neck-like structures are consistent with the notion that persistent loss of dynamins results in the trapping of intermediate vesicle-like structures that form during a process of NE protrusion but fail to timely undergo the fission step facilitated by dynamins. This role of dynamins (depicted in Supplementary Fig. 10) adds to the previously reported roles in fission of lysosomal tubules and of endocytic vesicles at the plasma membrane. Based on the ultrastructural cryo-ET data, long, narrow necks observed at the NE in the absence of dynamins are reminiscent of clathrin-coated pit necks at the plasma membrane in the same cells, and structures observed at the neuronal synapses[11,56]. Of note, neuronal synapses lacking dynamin contain (synaptic) vesicles, in addition to clathrin-coated pits[56], showing that membrane fission may occur without dynamin, yet not efficiently.

Importantly, we found that the vesicle-like structures contain γ-H2AX, which specifically associates with DNA DSBs, as well as the DNA-binding protein 53BP1, which facilitates non-homologous end joining
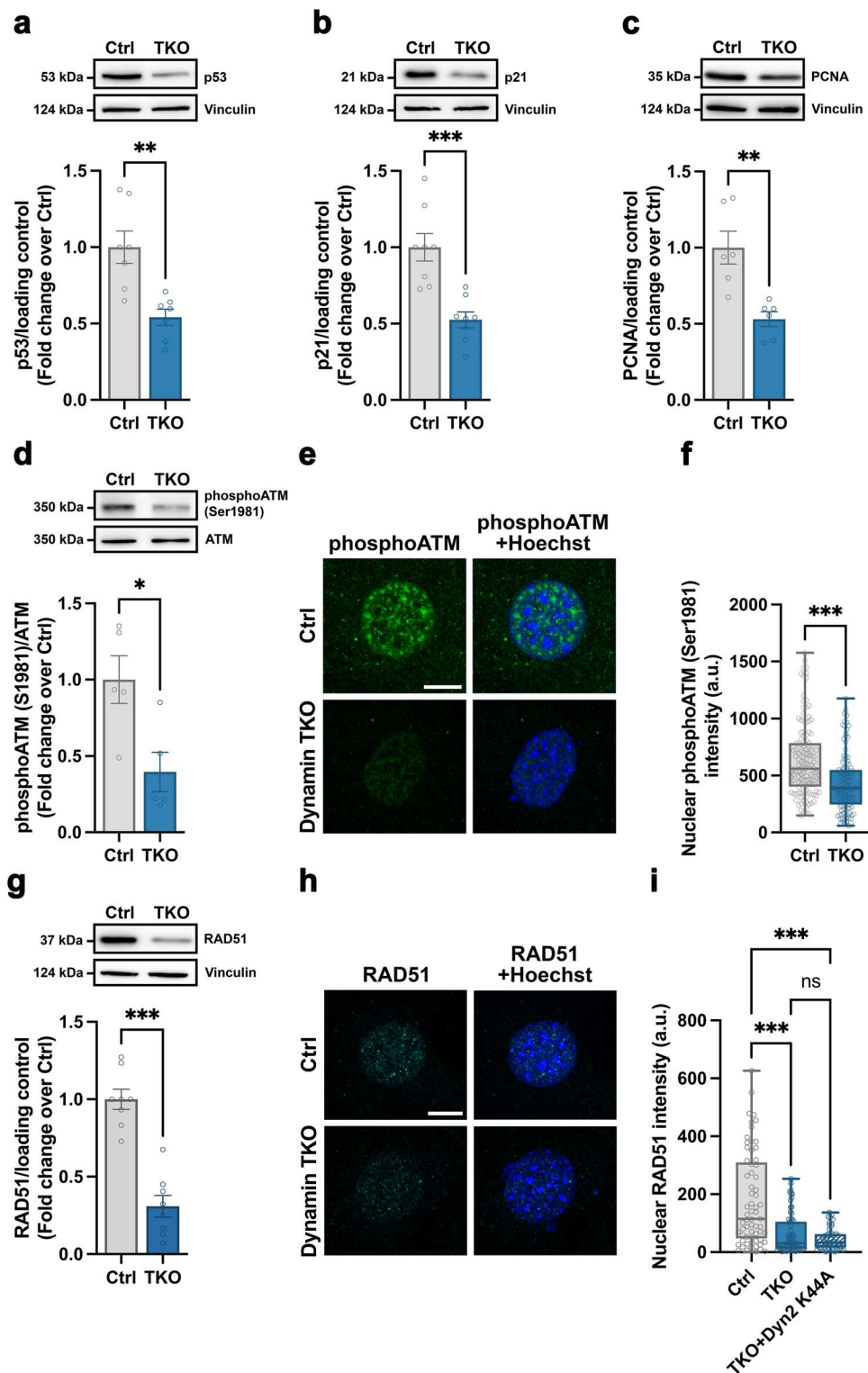
(NHEJ), and Rad51, which is required for homologous recombination repair (HR) of DNA. In addition, loss of dynamin resulted in a robust increase in γ-H2AX levels throughout the nuclear euchromatic compartment. Nuclear buds were identified as sites where DNA damage markers frequently accumulate. These findings suggest a cellular process for sequestering and possibly clearing damaged DNA material, and connect the process of nuclear membrane remodeling directly to genome maintenance and the DNA damage response.

A substantial body of evidence suggests that eukaryotic DNA repair is undertaken in discrete regions of the nucleus[57]. While DNA repair reactions can often occur in the immediate environment where damage was incurred, increased chromatin movement and lesion displacement to the nuclear periphery is a key feature of DNA repair of lesions requiring either HR or NHEJ[52]. Migration to the nuclear periphery is particularly observed for "hard-to-repair" lesions, such as those in telomeres or sites of replication stress[57]. Highly compacted heterochromatin, which is inherently difficult to repair, is usually already associated with the nuclear periphery. Recently, it has become clear that the NE itself can be highly mobile in cells, and DSB-capturing NE tubules (dsbNETs) driven by acetylated cytoplasmic microtubules

Fig. 6 | Absence of dynamin leads to compromised DNA damage repair.
a Western blot of p53 (top) and respective quantification (bottom). Seven biological samples/condition. **b** Western blot of p21 (top) and respective quantification (bottom). Eight samples/condition. **c** Western blot of PCNA (top) and respective quantification (bottom). Six samples/condition. **d** Western blot of phospho-ATM (residue Ser1981; top) and respective quantification (bottom). ATM (total) was used as a loading control. Five samples/condition. Representative images of phospho-ATM (Ser-1981 residue; green) and Hoechst (blue) stained nuclei in control and dynamin TKO cells (**e**), and respective quantification of nuclear phospho-ATM signal (**f**). Scale bar 10 μm. Three independent biological replicates; >126 cells/condition. **g** Western blot of RAD51 (top) and respective quantification (bottom). Eight samples/condition. Representative images of RAD51 (cyan) and Hoechst (blue) stained nuclei in control and dynamin TKO cells (**h**), and respective

quantification of nuclear RAD51 signal in control, dynamin-TKO, TKO expressing dynamin-2 and TKO expressing dynamin2-K44A for 24 h (**i**). Scale bar 10 μm. Three independent biological replicates; >51 cells/condition. Vinculin was used as a loading control in (**a**, **b**, **c**, **g**). Data are presented as bar charts with mean ± SEM, and as box plots showing the 25th percentile (Q1), median, 75th percentile (Q3), and whiskers extending to the minimum and maximum values; statistical significance is indicated as ns, not significant; ns, not significant; *$p < 0.05$; **$p < 0.01$; ***$p < 0.001$. Statistical analyses were performed using two-tailed unpaired Student's t test with Welch's correction (**a**: $p = 0.0040$, **b**: $p = 0.0008$, **c**: $p = 0.0056$, **d**: $p = 0.0185$, **g**: $p < 0.0001$), two-tailed Mann–Whitney U-test (**f**: $p < 0.0001$), and one-way ANOVA Kruskal–Wallis test followed by post-hoc Dunn's multiple comparisons test (**i**: $p < 0.0001$, $p > 0.9999$, $p < 0.0001$, respectively). a.u. Arbitrary units, Ctrl Control, TKO Triple knockout, WT Wild-type.

dynamically migrate to and recruit DSBs, together with associated repair proteins, for subsequent repair[53]. It follows that the NE buds and vesicles observed in dynamin-TKO cells may contain DNA damage/repair factors (together with their cognate damaged DNA) simply because the process of vesiculation fails to exclude damaged DNA associated with the NE. We observed that deliberately damaging DNA with CPT results in an increase in the number of NE buds/cell, suggesting that elevated levels of certain forms of DNA damage can induce NE vesiculation. Consistent with this notion, it has been recently shown that CPT-induced DNA damage gives rise to a transient increase in NE blebbing in human cells and that such CPT-induced lesions (termed TOP1cc) are eliminated in a process that requires functional selective autophagy[37]. Given that repair of TOP1cc depends on their exit out of the nucleus, we propose that dynamins play a role in the selective autophagy in DNA damage repair to ensure genome stability, as described in ref. 37, and that the process of NE vesiculation may be clinically relevant for cancer treatments and in other diseases, such as laminopathies, where NE dynamics play a role in the disease mechanism.

We detect the increased formation of autophagosomes in dynamin-TKO cells, yet their processing may be compromised. In agreement with this notion, defective autophagy has been shown to bring about a down-regulation of DNA damage response via the accumulation of p62/SQSTM1 and resultant loss of histone H2A ubiquitination required for recruitment of DNA repair machinery mediated epigenetic regulation[58], as well as loss of TWIST-mediated transcription of genes directly required for DNA repair[59], and regulation of the nuclear lamina[60]. Dynamin has been shown to be necessary for lysosomal biogenesis[33], and therefore, it cannot be excluded that lower lysosomal capacity in the absence of dynamins contributes to the accumulation of autophagosomes and possibly slows the processing of damaged DNA.

In our model, dynamins participate in the final scission step that allows the budding of NE vesicles containing cargo destined for autophagic destruction/recycling. Our finding that DNA repair factors involved in both HR and NHEJ are found within putative precursors of these vesicles suggest that irreparably damaged (or otherwise unwanted) DNA generated during DNA repair processes constitutes one cargo. A prediction of our model would be that failure to remove unwanted/damaged DNA via selective autophagy would result in increased levels of genomic instability. Interestingly, autophagy-deficient cells and tissues display increased levels of unresolved DNA damage, chromosome instability, gene amplification and aneuploidy[61–63] and monoallelic loss of the autophagy regulator beclin 1 is routinely observed in cancers such as breast carcinoma[61].

Recently, Herve et al. described a mechanism wherein chromosomal aberrations arising during mitosis result in NE defects triggering an ATR-dependent cell cycle arrest—the NE mechano-sensitive checkpoint[64]. Although loss of dynamins clearly gives rise to NE dysmorphisms, dynamin-TKO does not appear to trigger this checkpoint, as dynamin-TKO cells did not induce the accumulation of either the

checkpoint protein p53 or the CDK inhibitor p21. This suggests that dynamin may be dispensable for the NE mechano-sensitive checkpoint. We nonetheless cannot rule out that indirect consequences of dynamin absence, such as during mitosis, may contribute to the phenotype reported in this study. Speaking in favor of the dynamin superfamily direct role is also a recent electron tomography-based study in yeast, which indicates that Dnm1 is involved in nucleophagy[17]. These findings further underscore the potential involvement of the dynamin family in preserving NE structure and function, bridging their well-known roles in membrane dynamics with NE homeostasis.

Notably, the induction of nuclear dysmorphisms by dynamin inhibition (dynasore) and mutant K44A expression in WT cells points to a proximal effect of dynamin dysfunction on NE architecture. While we note transient accumulation of dynamin-2 in the nuclear proximity, this study does not provide direct evidence for the physical engagement of dynamins with the NE. Despite technical challenges in visualizing transient, low-abundance membrane interactions, several complementary experiments suggest that dynamins may transiently associate with the NE. First, we detect dynamin – a cytosolic protein that typically associates with cytoplasm-facing membranes – in the nuclear fraction. Second, reintroduction of dynamin-2 into dynamin-TKO cells rescues NE dysmorphisms within hours after dynamin-2 reintroduction. Third, expression of the GTPase-deficient mutant dynamin-2 K44A – which retains the membrane-binding capacity domain but becomes "locked" on membranes due to impaired GTP hydrolysis – leads to the accumulation of fluorescent signal near NE buds. We intentionally avoided using ONM markers such as full-length nesprin (of the LINC complex), given that overexpression of nesprin-3 perturbed NE organization and dynamics in our hands.

Lastly, our study also reveals, unexpectedly, that treatment with nocodazole, a microtubule-disrupting agent, reverses both the nuclear shape abnormalities and the accumulation of DNA damage in dynamin-deficient cells. This points to a complex interplay between dynamins, the microtubule cytoskeleton, and the maintenance of nuclear and genome integrity. It further suggests that aberrant microtubule dynamics contribute to the pathology observed when dynamins are absent.

In sum, our data suggest a delay in the fission mechanisms from the ONM in the absence of dynamins (Drp1 is not altered in dynamin-TKO cells[19]) that may allow for the build-up of additional membrane and cargo (e.g., damaged DNA). Given that loss of dynamins results in decreased lamins and some DNA repair proteins, nuclear dysmorphisms and accumulation of DNA damage, our data suggest that dynamin is a key upstream component of NE and DNA homeostasis. Taken together, we propose that dynamins, through their interaction with microtubules, have a key role in the NE homeostasis and, likely indirectly, in maintaining genome stability. Future studies may be directed towards understanding the regulation of fission mechanisms at the NE, and which other factors besides dynamins and microtubules (e.g., torsins[65]) may be at play. Besides cancer and neurodegenerative diseases, our findings have significant implications for the aging
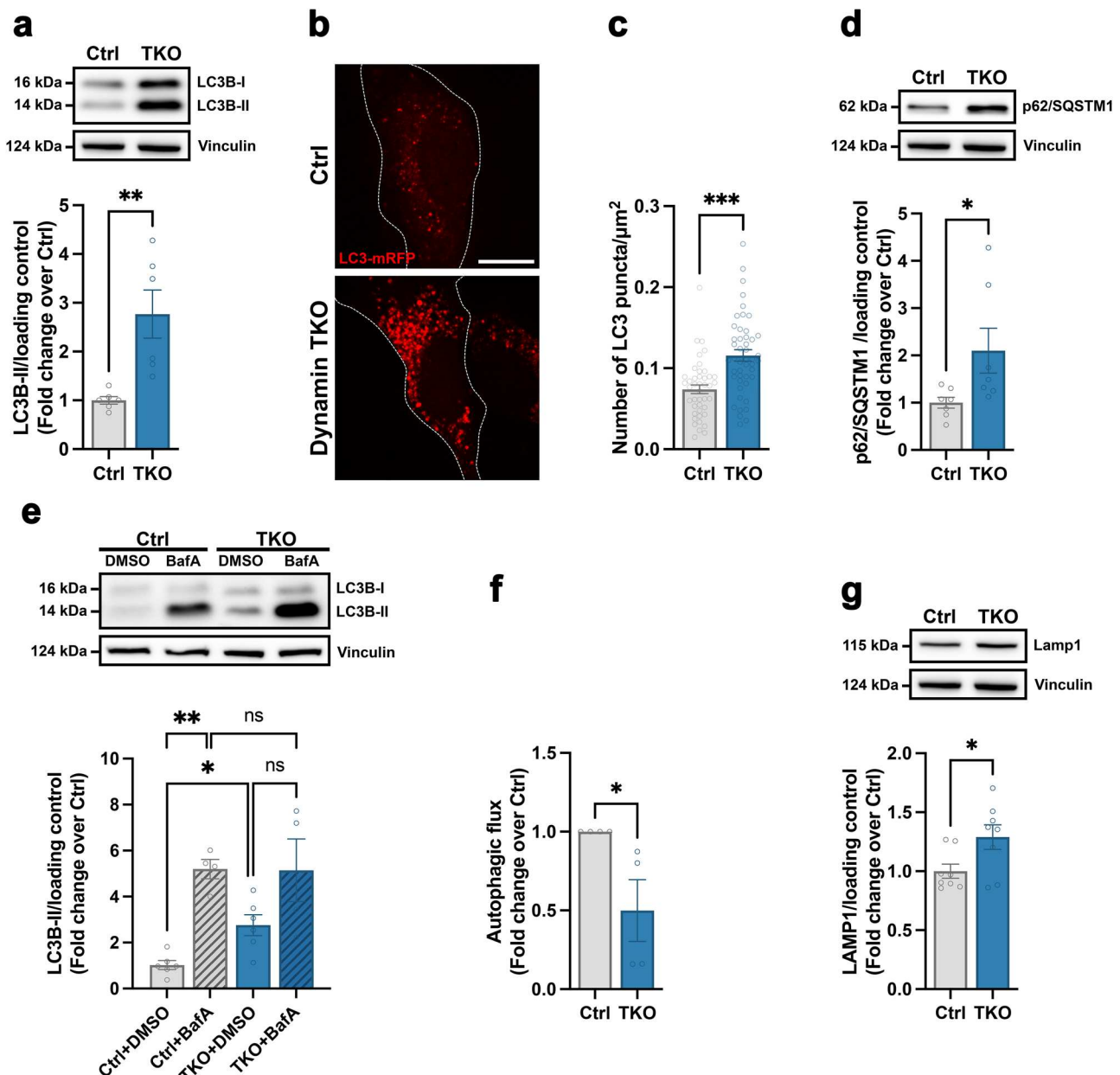
Fig. 7 | Dynamin TKO cells accumulate autophagosomes. a Western blot of LC3B (top) and respective quantification (bottom). Vinculin was used as a loading control. Six samples/condition. Representative confocal images of control and dynamin-TKO cells transfected with LC3-mRFP for 24 h (**b**) and quantification of LC3 puncta number (**c**). Scale bar, 20 μm. Three independent biological replicates; $n > 43$ cells/condition. **d** Western blot of p62/SQSTM1 (top) and respective quantification (bottom). Vinculin was used as a loading control. Six samples/condition. **e, f** Autophagic flux analysis in control and dynamin TKO cells. Western blot of LC3B (top) and respective quantification (bottom) in control and dynamin TKO cells in the presence or absence of Bafilomycin A (BafA, 100 nM; 6 h), a lysosomal degradation inhibitor (**e**). Vinculin was used as a loading control. Four samples/condition.

Autophagic flux was determined in the presence of the lysosomal inhibitor Bafilomycin A and calculated by subtracting the densitometric value of LC3B-II-BafA from those corresponding LC3B-II + BafA values (**f**). **g** Western blot of LAMP1 (top) and respective quantification (bottom). Vinculin was used as a loading control. Eight samples/condition. Data are presented as bar charts with mean ± SEM, ns, not significant; *$p < 0.05$; **$p < 0.01$. Statistical analyses were performed using two-tailed unpaired Student's t test (**c**: $p < 0.0001$), two-tailed Mann–Whitney U-test (**e**: $p = 0.0286$; **f**: $p < 0.0001$), and one-way ANOVA followed by post-hoc Dunnett's multiple comparisons test (**d**: $p = 0.2626$, $p = 0.3746$, $p = 0.0023$, $p > 0.9999$). a.u. Arbitrary units, Ctrl Control, TKO Triple knockout, WT Wild-type.
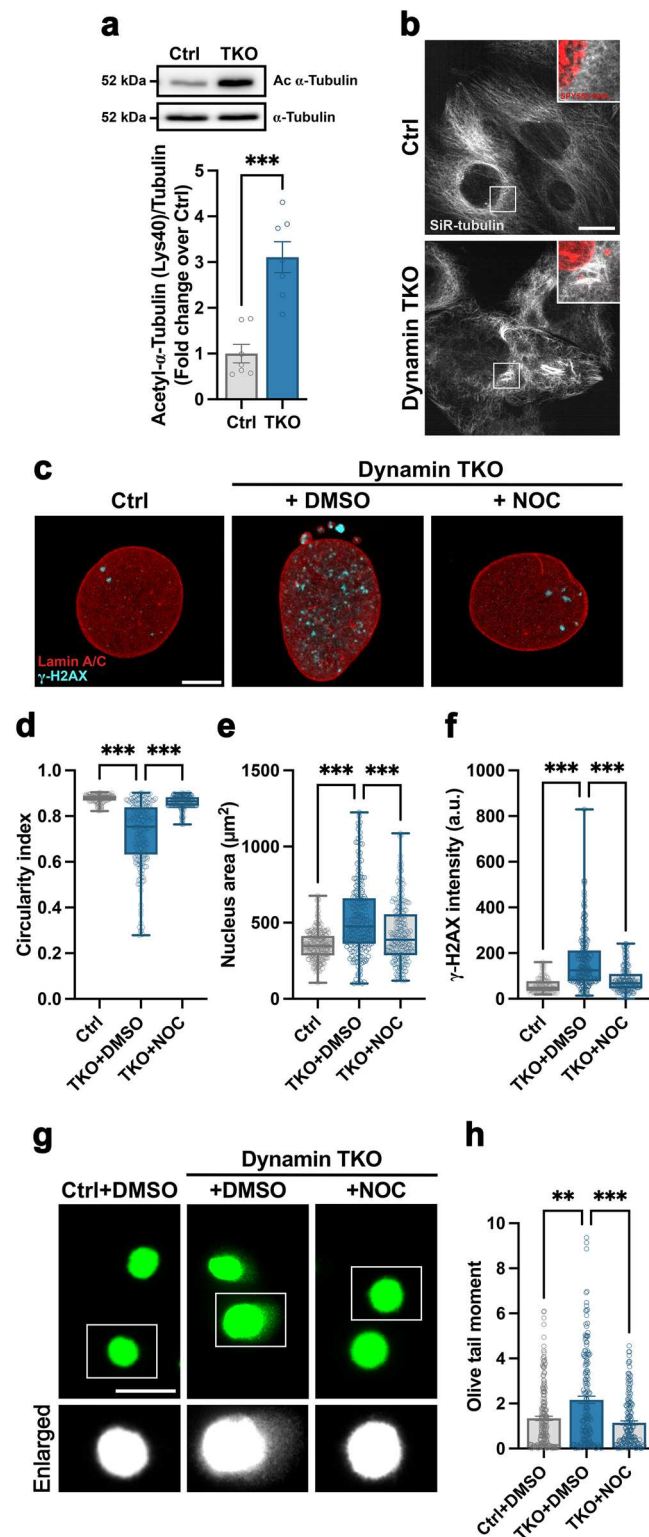
research[18] and may pave the way towards a better understanding of aging mechanisms and safeguards against aging-associated cellular decline.

Methods
Cell lines and generation of dynamin TKO cells
Dynamin 1,2,3 triple knockout (TKO) mouse fibroblasts[20], a kind gift from Pietro de Camilli (Yale University, New Haven, USA), were generated by inducing deletion of all three dynamin genes in cultured cells using 4-hydroxytamoxifen (4-OHT; Sigma-Aldrich)[19,20]. Wild-type (WT) mouse (C57BL/6J) fibroblasts were obtained from ATCC (SCRC-1008). Dynamin TKO mouse fibroblasts and WT mouse fibroblasts were cultured in the growth medium: high glucose Dulbecco's Modified Eagle Medium (DMEM; Sigma-Aldrich) supplemented with 1% Penicillin-Streptomycin (Gibco) and 10% Fetal Bovine Serum (FBS; Gibco), and maintained at 37 °C in a humidified atmosphere with 5% CO_2. Cells were passaged at ~80% confluence and used (up to passage 60) in various experiments as described below. Unless otherwise stated, cells

Fig. 8 | Nocodazole treatment restores nuclear envelope morphology and diminishes DNA damage. a Western blot of acetylated α-tubulin (top; residue Lys40), and respective quantification. Normalized to α-Tubulin (bottom). Vinculin was used as a loading control. Seven biological samples/condition. **b** SiR-tubulin and SPY555-DNA™ stained control and dynamin TKO live cells. Scale bar 20 μm; insets 14 μm. Three independent biological replicates. Representative images of lamin A/C and γ-H2AX immunostained nuclei in control and dynamin TKO cells treated with DMSO (control) or nocodazole (**c**), and respective quantification of nuclear circularity (**d**), nuclear area (**e**) and γ-H2AX signal (**f**). Scale bar 10 μm. Four independent biological replicates; >180 cells/condition. Representative images of control and dynamin TKO cells treated with nocodazole analysed by alkaline comet assay (**g**), and respective quantification of DNA damage (**h**; Olive tail moment = [tail mean-head mean] × % of DNA in the tail). Scale bar 50 μm; insets 90 μm. Three independent biological replicates, >164 cells/condition. Data are presented as bar charts with mean ± SEM, and as box plots showing the 25th percentile (Q1), median, 75th percentile (Q3), and whiskers extending to the minimum and maximum values; statistical significance is indicated as **$p < 0.01$; ***$p < 0.001$. Statistical analyses were performed using two-tailed Student t test with Welch's correction (**a**: $p = 0.0003$), one-way ANOVA Kruskal–Wallis test followed by post-hoc Dunn's multiple comparisons test (**d**: $p < 0.0001$, $p < 0.0001$, **e**: $p < 0.0001$, $p < 0.0001$, **f**: $p < 0.0001$, $p < 0.0001$, **h**: $p = 0.0019$, $p = 0.0002$). Ac Acetylated, a.u. Arbitrary units, Ctrl Control, NOC Nocodazole, TKO Triple knockout.

lentiviral packaging was obtained from Takara Bio and maintained at 37 °C in a humidified atmosphere with 5% CO_2 in high glucose DMEM supplemented with 1% Penicillin-Streptomycin and 10% FBS.

Cell treatments

Dynamin control and TKO cells (at 12 days) were treated with DMSO as a control (Fisher), and 1 μm MG132 (InVivoGen) or 100 nM of Bafilomycin A (BafA; Santa Cruz Biotechnology) for 6 h at 37 °C. Dynamin control and TKO cells (at 11 days) were treated with DMSO as control (Fisher), or 100 nM nocodazole (NOC; Sigma-Aldrich) for 24 h at 37 °C. Dynamin control and TKO cells (at 12 days) were treated with DMSO as control (Fisher) or 50 nM camptothecin (CPT; Sigma-Aldrich) for 30 min. WT mouse fibroblasts and human primary fibroblasts were treated with DMSO or 40 μM dynasore (Sigma-Aldrich) for 24 h at 37 °C.

Site-directed mutagenesis

Mutations R361S (Arg361Ser) and R399A (Arg399Ala) were introduced into *DNM2* coding sequence using Q5 site-directed mutagenesis (New England Biolabs, NEB), following the manufacturer's instructions with minor alterations. Plasmid templates were quantified by spectrophotometry (NanoDrop One, Thermo Fisher Scientific). PCR amplification was performed with mutagenic primers (see Supplementary Information) using Phusion High-Fidelity DNA polymerases (#F530S, Thermo Fisher Scientific) under the following cycling conditions: 98 °C for 60 s; 25 cycles of 98 °C for 10 s, 70 °C (R361S) or 59 °C (R399A) for 20 s, and 72 °C for 150 s; followed by 72 °C for 10 min. The amplified products were treated with KLD enzyme mix (NEB) at room temperature (RT) for 15 min. Following transformation into chemically competent *E. coli* (NEB), bacteria were plated on LB agar supplemented with the appropriate antibiotics and incubated overnight at 37 °C. Single colonies were selected and grown in LB media for plasmid isolation using NucleoSpin plasmid mini kit (Macherey–Nagel). The presence of the desired mutations was verified by Sanger sequencing. Clones confirmed to carry the correct mutations were tested by digestion with restriction enzymes and selected for subsequent experiments.

Lentiviral production

Lentiviruses were produced by transfecting Lenti-X 293T with the transfer plasmid containing the insert of interest flanked by the viral LTR and combined with the CMV-pAmphoR envelope and CMV-Δ8.2R packaging plasmids. Transfection was performed using

were used after 12 days of the 4-OHT treatment, and the efficiency of each treatment was verified by Western blotting against all three dynamins using the pan-dynamin antibody (BD Transductions Laboratories). For every 4-OHT treatment, a passage-matched control was used. Primary cultures of human dermal fibroblasts obtained from a skin biopsy of a healthy individual (ATCC PCS-201-012) were also used. These cells were cultured in high-glucose DMEM supplemented with 15% FBS, 2 mM L-glutamine (Gibco) and 1% Penicillin-Streptomycin, and maintained at 37 °C and 5% CO_2. Lenti-X 293T used for

polyethylenimine (PEI; DNA:PEI ratio 3 µg:1 µl). Fifty hours post-transfection, the virus-containing supernatant was harvested, centrifuged at $1000 \times g$ to remove cells, and then filtered through a 0.45 µm polyvinylidene fluoride (PVDF) filter. For viral transduction, control and dynamin-TKO cells were incubated with the viral supernatant for 24 h at 37 °C.

Cell transfections
In addition to lentiviral transduction, plasmids were introduced into cells by electroporation (Amaxa 4D-Nucleofector X Unit, Lonza), using the P4 4D NucleofactorTM kit (Lonza), following the manufacturer's instructions. The cell suspension (-0.8 × 10⁶ cells) was pelleted by centrifugation for 5 min at $500 \times g$ and the cell pellet resuspended in 100 µL P4 Primary Cell Nucleofector™ Solution. 1–2 µg plasmid DNA was gently mixed with the cells and transferred to the Nucleocuvette, avoiding air bubbles. Electroporation was then carried out using the 4D-Nucleofector™ X Unit with program CZ-167. Cells were transferred to growth medium, plated on coverslips in a 12-well plate, and maintained at 37 °C with 5% CO_2. Unless otherwise stated, cells were used for experimentation 24 h post-transfection.

Western blotting
Cells were lysed on ice in RIPA buffer (50 mM Tris-HCl, pH 7.4, 150 mM NaCl, 5 mM EDTA, 1% Triton X-100, 0.5% deoxycholate, 0.1% sodium dodecyl sulfate/SDS) supplemented with protease/phosphatase inhibitors and 1 mM dithiothreitol (DTT). Lysates were incubated on ice for 30 min, and insoluble material was removed by centrifugation (10 min, 16,000 g, 4 °C). Protein concentration was measured using the BCA assay (Pierce). Samples were denatured in sample buffer (6x: 0.5 M Tris, 30% glycerol, 10% SDS, 0.6 M DTT, 0.012% bromophenol blue) at 95 °C for 5 min and stored at −20 °C. Proteins were separated by SDS–PAGE on custom 6-10% polyacrylamide gels (BioRad) and transferred to Immobilon-P PVDF membranes (Amersham, Cytiva). Membranes were blocked in 5% milk or bovine serum albumin (BSA) in TBST for 1 h at RT and incubated overnight with primary antibodies (1:1000) in TBST containing 5% milk or BSA. After washing, membranes were incubated with horseradish peroxidase (HRP)-linked anti-mouse or anti-rabbit IgG secondary antibodies (1:5000) for 1 h at RT. Bands were visualized by enhanced chemiluminescence using ECL substrate on an ImageQuant 8000 system (Amersham, Cytiva). Membranes were re-probed with anti-vinculin (1:10,000; Sigma) as a loading control. Band optical density was quantified using Image Lab (BioRad), normalized to the loading control, and reported relative to the experimental control.

Autophagic flux measurement by LC3B turnover assay
The LC3B turnover assay quantifies the amount of LC3B-II delivered to lysosomes by comparing LC3B-II levels in the presence and absence of the lysosomal inhibitor Bafilomycin A (BafA; 100 nM) via Western blotting. Autophagic flux in control and dynamin TKO cells was quantified as the difference between LC3B-II densitometric values in BafA-treated and BafA-untreated samples. For each independent experiment, the subtracted values for each condition were normalized to those of the control cells. The results are presented as the mean values for each experimental condition.

Nucleus and cytoplasm isolation from cultured cells
Cytosolic and nuclear extracts were performed using the REAP cell fractionation protocol[66].

Immunocytochemistry and image acquisition
For fixed-cell imaging, cells were grown on gelatin-coated coverslips, washed with pre-warmed PBS (pH 7.4), and fixed with 4% PFA for 20 min at RT. After washing, cells were permeabilized with 0.1% Triton X-100/PBS for 10 min at RT, washed again, and blocked with 3% BSA/

10% goat serum/PBS for 1 h at RT. Cells were then incubated overnight at 4 °C with primary antibodies diluted in blocking solution: mouse anti-lamin A/C (1:750), rabbit anti-γ-H2AX (1:500), rabbit anti-phospho-ATM (1:250), and rabbit anti-RAD51 (1:100). After three PBS washes, cells were incubated for 1 h at RT with Alexa Fluor 488-, 568-, or 647-conjugated goat anti-mouse or anti-rabbit IgG secondary antibodies. Nuclei were stained with Hoechst 33342 (2 µg/mL; Invitrogen), and coverslips were mounted with Mowiol 4-88. Antibody specificity was confirmed by immunoblotting and secondary-only controls lacking primary antibodies.

Nucleus imaging acquisition and data analysis
Fixed samples were imaged using a confocal microscope (LSM 710, Carl Zeiss) with an Axio-Observer Z1 and Plan-Apochromat 63×/1.4 oil DIC M27 objective, or a Zeiss Axio Scan.Z1 slide scanner with a Plan-Apochromat 20×/0.8 objective, operated via ZEN software. Live samples were imaged on a custom-built spinning disk confocal microscope (Perkin Elmer/Nikon/Velocity) equipped with a temperature-controlled custom imaging chamber[67].

Post-acquisition image analysis and processing were performed using both ZEN and ImageJ/Fiji. NE morphology analyses were performed in lamin A/C-immunolabelled cells, as well as live cells expressing GFP-Lamin-A. Quantification of dysmorphic nuclei percentage was done in a blinded manner by direct manual (visual) counting of positive misshapen nuclei in 40 randomly chosen non-overlapping fields (×630 magnification; acquired by Axio Observer Z1), normalized to the total number of nuclei stained with Hoechst 33342 for each experimental condition. Results are represented by the mean ± standard error of the mean (SEM) of four independent experiments (>400 cells analysed per experimental condition) and are expressed as a percentage of control cells. Nuclear phenotypes in control and dynamin-TKO cells were analyzed manually in a blinded manner, based on the literature and by following predefined parameters. To be classified as a lamin A/C–positive vesicle, a structure had to be clearly separated from the nucleus and distinguished from micronuclei based on its interphase origin, higher abundance (typically >3 lamin A/C–positive structures/cell), and smaller size (≤1/100 of the nuclear area in fluorescence images). In contrast, micronuclei typically arise during mitosis, are fewer in number (1–3 per cell), and are larger in size (up to 1/10 of the nuclear area). Structures meeting the above criteria but remaining continuous with the nucleus were classified as nuclear buds.

The percentage of the different nuclear phenotypes was performed by direct manual counting of the respective misshapen nuclei in 2 random non-overlapping fields of an entire coverslip imaged by the Zeiss Axio Scan.Z1 slide scanner system. Results are presented as mean ± SEM from at least three independent experiments (>3000 cells per condition) and expressed as a percentage of control. Nuclei morphology was analyzed from z-projected confocal images of lamin A/C–stained nuclei using the Fiji plugin[68]. For each independent experiment, 20–30 randomly chosen, non-overlapping fields (x630 magnification) were acquired per condition. Briefly, images were thresholded, and nuclei were automatically detected based on size (100-infinite) and circularity (0.3–1). For each identified nucleus, area, perimeter, and circularity ($4\pi \times$ area/perimeter²) were measured.

For quantification of nuclear γ-H2AX, phospho-ATM, and RAD51 levels, z-stack confocal images of stained nuclei were acquired, and the resulting z-projected images were analysed in Fiji. For each independent experiment, 15–30 randomly selected, non-overlapping fields (×630 magnification) were imaged per condition. Nuclei were automatically detected as described above as described above and defined as region of interest (ROI). The mean γ-H2AX, phospho-ATM, and RAD51 fluorescence intensities within the ROI were then quantified using Fiji.

Assessment of nuclear envelope integrity using NLS-mCherry reporter

To evaluate NE integrity, cells were transfected (at 11 days) with an pmCherry-nuclear localization signal (NLS) reporter plasmid. After 24 h, cells were washed with pre-warmed PBS (pH 7.4) and fixed with 4% (w/v) paraformaldehyde (PFA) for 20 min at RT. Then, the NE was labeled using an anti-lamin A/C (1:750), followed by the secondary antibody Alexa Fluor 647-conjugated goat anti-mouse IgG, as described in the "Immunocytochemistry and image acquisition" section. Nuclei were stained with Hoechst 33342 (2 μg/mL; Invitrogen Molecular Probes).

NE integrity was assessed by the localization of mCherry-NLS: nuclear-restricted fluorescence indicated an intact NE, whereas cytoplasmic or diffuse signal suggested compromised NE integrity. Lamin A/C immunostaining was used to delineate nuclear contours and assess NE morphology. The percentage of ruptured nuclei was determined by direct counting of the mCherry-NLS positive cells with cytosolic signal, normalized to the total number of positive mCherry-NLS cells, in 4 random non-overlapping fields of an entire coverslip imaged by the Zeiss Axio Scan.Z1 slide scanner system. Results are represented as the mean ± SEM of three independent experiments (>382 cells analysed for each condition).

Alkaline comet assay

This assay was performed as in Singh et al.[45], with modifications. The cells were detached by trypsinization and diluted to a concentration of 0.2×10^6 cells/mL. 50×10^3 cells were added to 1 mL fresh preheated 1% (w/v) low-melting-point agarose (BioRad). Cells resuspended in agarose were transferred onto a Superfrost Plus microscope slide (VWR) pre-coated with 1% (w/v) normal melting point agarose (Biozym) and covered with a coverslip. The slides were placed in the dark on an ice-cooled metal plate to solidify. Once the agarose solidified, coverslips were removed from the slides, and slides were incubated horizontally in fresh, cold alkaline lysis buffer (2.5 M NaCl, 100 mM EDTA disodium salt, 10 mM Tris-Base, 200 mM NaOH in dH$_2$O, completed just prior to use by adding 1% (v/v) DMSO and 1% (v/v) Triton X-100) in the dark at 4 °C for 6 h. Slides were then immersed horizontally in fresh, pre-chilled electrophoresis buffer (6% (v/v) 5 M NaOH, 0.5% 200 mM EDTA, 1% DMSO in dH$_2$O, pH>13) for 30 min in the dark, to allow DNA unwinding. Electrophoresis was conducted for 25 min at 1 V/cm (25 V) and current adjusted to 300 mA; after which the slides were washed twice in neutralization buffer (500 mM Tris-Base in dH$_2$O, adjusted to pH 8-8.1 by HCl addition) for 5 min each. Slides were incubated in cold 70% Ethanol for 5 min and allowed to air dry in the dark. Once dry, slides were rehydrated by immersion in warm TE buffer (1 mM EDTA, 10 mM Tris-HCl in dH$_2$O) and stained with 0.1% (v/v) SYBR Gold (Sigma-Aldrich) in TE buffer for 15 min. The stain was rapidly washed by dipping slides in dH$_2$O, and slides were air-dried before imaging. Positive control cells were treated with 1 mM H$_2$O$_2$ in the growth medium for 30 min at 37 °C prior to trypsinisation. To avoid light-induced DNA damage, the assay was performed without exposure to direct artificial light, with all incubation and drying steps carried out in the dark.

Comet assay images were acquired in the GFP channel using an EVOS™ M5000 microscope (Invitrogen) at ×20 magnification. Imaging parameters were kept constant across all conditions and experiments. Image analysis was performed using the open-source software OpenComet[69]. Comets exhibiting edge artifacts, clumped heads or tails, or poor segmentation quality (observed equally across all conditions) were excluded from analysis. Threshold settings were maintained consistently across images to ensure standardization. The Olive Tail Moment, defined as (tail mean − head mean) × % DNA in the tail and considered the most reliable indicator of DNA damage in the Comet assay[70], was systematically quantified for all datasets.

Cell culture for cryo-ET

Two hundred mesh R2/2 gold finder grids (Quantifoil) were glow-discharged in an air atmosphere for 45 s on high power using a Harrick plasma cleaner. The grids were then immersed in a solution of fibronectin at 20 ng/ml, deposited in a 6-well plate and incubated in a droplet of fibronectin for an extra 30 min. Grids were washed twice with PBS (Gibco), and 3 mL dynamin-TKO cells at 1×10^5 cells/mL in the growth medium were added on top of the grids and left overnight. The next morning, the cells were stained using SPY555-DNA (Spirochrome) for 2 h in the growth medium. After a media change, the grids were plunge frozen using a Leica GP2 (Leica). Vitrified grids were then clipped into autogrids (ThermoFisher Scientific) and subsequently stored in liquid nitrogen.

Electron microscopy

To preserve membrane and structure integrity, cells were fixed using high-pressure freezing fixation. Control and dynamin-TKO cells attached to 3 mm coverslips were put in a small volume of cryoprotectant solution (20% BSA in piperazine-N,N′-bis(2-ethanesulfonic acid) buffer) and high-pressure frozen using a Leica EM ICE. Frozen samples were transferred under liquid nitrogen to a Leica EM AFS2 freeze-substitution unit and processed as in ref. 71, with the following modifications: the freeze substitution medium was 0.2% uranyl acetate and 5% water in acetone, the resin used was Lowicryl HM20 Monostep (PolySciences), and the UV polymerization schedule was 24 h at −45 °C, warm to 0 °C during 12 h, then 36 h at 0 °C. 90 nm sections were transferred to 50 mesh formvar-coated Cu grids and post-stained for 5 min with Reynolds lead citrate, washed and air dried, and then imaged on the JEOL 1400 TEM as above.

Cryo-focused ion beam (FIB) milling

Autogrid-clipped TEM grids were inserted into a cassette and loaded into the Plasma FIB Arctis microscope (ThermoFisher Scientific). Identification of lamella sites and milling were then carried out using the webUI v1.1 software (Thermo Fisher Scientific). Briefly, an SEM tile set of the grid was used to identify cells suitable for milling. For each identified cell, a reflection and green–red fluorescence z-stack was acquired over ±7.5 μm in 0.5 μm steps using the chamber microscope, and this stack was used to guide lamella template positioning. The grid was then coated with organo-platinum using the gas injection system for 50 s and then sputter-coated with platinum metal for 120 s. For each site, electron centering of the fluorescent target, followed by eucentric height and milling angle search (12° target), was performed before positioning a 15 μm width lamella milling template. Milling was performed at 30 kV using Argon gas to generate plasma and a targeted final lamella thickness of 150 nm. For each site, stress-relief cuts on both sides of the intended lamella were first milled with a 0.74 nA ion beam, followed by three milling steps at 0.74 nA, 0.2 nA and 60 pA to obtain a ~400 nm thick lamella. After completing the three milling steps for all sites, the ~400 nm lamellae were polished with a 20 pA beam to a target thickness of 150 nm. A final reflection and red–green fluorescence z-stack (± 7.5 μm, 0.5 μm steps) was then acquired for each polished lamella, followed by a 5-s platinum sputter coat before returning the autogrid to the cassette.

Cryo-ET data acquisition and processing

Cryo-ET data were acquired on a G3i Titan Krios equipped with a Falcon 4i and Selectris-X energy filter. The PACEtomo_targetsFromMontage_v0.13.py script[72] was used inside SerialEM 4.1beta (https://bio3d.colorado.edu/SerialEM/) to add targets from medium mag montages acquired at 15,000x magnification. The PACEtomo_measureOffset.py script was used to measure and calculate the tilt axis offset value optimized for the z-movement of the sample. For the correlation, medium magnification montages were saved as single images and imported into MAPS version 3.25 for manual correlation.

After setup, the PACEtomo.py script was used to collect selected targets in parallel with beam-tilt compensation, employing a dose-symmetrical tilt scheme of ±54° in 3° increments, starting at −12° to account for lamella pretilt. Tilt-series were recorded at a nominal magnification of ×64.000, resulting in a pixel size of 1.9026 Å, with 3.24 e⁻/Å² per tilt, across 6 frames, leading to a total dose of ~116 e⁻/Å².

Data were pre-processed using the RELION-5.0 beta (https://github.com/3dem/relion/tree/ver5.0). MRC files were motion-corrected using the Relion motion correction algorithm using half map creation for downstream denoising, and CTF was estimated with CTFFIND4 version 4.14[73]. Tomograms for initial visualization were reconstructed using automated reconstruction in AreTomo version 1.3.3[74] while reconstructions from RELION-5.0 beta were used for denoising using CryoCARE[75]. Membrane segmentation was carried out on denoised tomograms using the standard MemBrain-Seg protocol[76]. Segmentations were trimmed using IMOD[77] before visualization in ArtiaX[78,79], in ChimeraX[80].

TUNEL, propidium iodine/AnnexinV-FITC, trypan blue exclusion and cleaved caspase-3 assays

The proportion of apoptotic cells in control and dynamin-TKO cultures was determined using the DeadEnd™ Fluorometric TUNEL system kit (Promega) following the manufacturer's instructions, with minor modifications detailed in the Supplementary Information. For propidium iodide (PI)/Annexin V–FITC staining, control and dynamin-TKO cells were cultured on coverslips overnight and stained according to the manufacturer's protocol (Thermo Fisher, V13242). Cell viability was further assessed by trypan blue exclusion, where dead cells are stained blue and live cells remain unstained; equal numbers of control and dynamin-TKO cells were mixed 1:1 with trypan blue and counted using a Countess 3 automated cell counter (Invitrogen). Protein levels of cleaved caspase-3 were measured by western blotting using a rabbit anti–cleaved caspase-3 antibody (1:1,000), and details of the immunofluorescence assay are provided in the Supplementary Information.

Additional methodological information is provided in the Supplementary Methods in the Supplementary Information file. All reagents and plasmids are listed in Supplementary Table 1.

Statistics and reproducibility

Unless otherwise specified, statistical analyses were done using and GraphPad Prism versions 8.0.1 and 10.2.0 and Microsoft Excel Microsoft version 16.89.1. For fluorescence imaging data displayed as box plots with individual cells shown, outliers were identified using the ROUT test, which fits the data with nonlinear regression and applies a 1% false discovery rate (Q) to pooled experimental replicates. Identified outliers were excluded from subsequent analysis. Normality (Gaussian distribution) was tested using the Shapiro–Wilk test. For comparisons between two groups with Gaussian distributions, unpaired (two-tailed) Student's t tests were conducted (with Welch's correction in case of unequal variances), whereas Mann–Whitney U-tests were used to test the statistical difference of two groups with non-Gaussian distributions. Comparisons between multiple groups ($n > 2$) with non-gaussian distributions was performed using Kruskal–Wallis one-way analysis of variance (ANOVA) followed by post-hoc Dunn's multiple comparisons test to test the statistical difference between groups, or Brown Forsythe and Welch ANOVA followed by post-hoc Dunnett's test for groups with gaussian distribution and unequal standard deviations, or two-way ANOVA followed by Tukey's post-hoc test. A p value lower than 0.05 was considered statistically significant, and significance levels were indicated with *$p < 0.05$; **$p < 0.01$; and ***$p < 0.001$. Results are expressed as mean ± SEM. For each experiment and treatment, an appropriate experimental group was defined, with exact sample sizes, statistical tests, biological replicates, and key experimental details provided in the figure legends. Imaging and Western blotting experiments included at least three independent replicates (often more, see

Figure legends), with one biological sample per condition per experiment. No randomization into experimental groups was performed prior to freezing for EM experiments. Investigators were blinded during data acquisition and analysis when feasible. However, the pronounced differences between conditions sometimes made blinding ineffective, so selective imaging analyses were independently performed by 2–3 investigators across two institutions.

Data availability

Key primary and all secondary data are included in the paper and Supplementary Information file, Source data, as well as the reporting summary. The newly generated constructs, and additional primary data (a part of still ongoing collaborative study) are available from the corresponding author. Source data are provided with this paper.

References

1. Gruenbaum, Y. & Foisner, R. Lamins: nuclear intermediate filament proteins with fundamental functions in nuclear mechanics and genome regulation. *Annu. Rev. Biochem.* **84**, 131–164 (2015).
2. Kalukula, Y., Stephens, A. D., Lammerding, J. & Gabriele, S. Mechanics and functional consequences of nuclear deformations. *Nat. Rev. Mol. Cell Biol.* **23**, 583–602 (2022).
3. Shah, P., Wolf, K. & Lammerding, J. Bursting the bubble—nuclear envelope rupture as a path to genomic instability? *Trends Cell Biol.* **27**, 546–555 (2017).
4. Pathak, R. U., Soujanya, M. & Mishra, R. K. Deterioration of nuclear morphology and architecture: a hallmark of senescence and aging. *Ageing Res. Rev.* **67**, 101264 (2021).
5. Karoutas, A. & Akhtar, A. Functional mechanisms and abnormalities of the nuclear lamina. *Nat. Cell Biol.* **23**, 116–126 (2021).
6. Shpetner, H. S. & Vallee, R. B. Identification of dynamin, a novel mechanochemical enzyme that mediates interactions between microtubules. *Cell* **59**, 421–432 (1989).
7. Shpetner, H. S. & Vallee, R. B. Dynamin is a GTPase stimulated to high levels of activity by microtubules. *Nature* **355**, 733–735 (1992).
8. Scaife, R. & Margolis, R. L. Biochemical and immunochemical analysis of rat brain dynamin interaction with microtubules and organelles in vivo and in vitro. *J. Cell Biol.* **111**, 3023–3033 (1990).
9. Maeda, K., Nakata, T., Noda, Y., Sato-Yoshitake, R. & Hirokawa, N. Interaction of dynamin with microtubules: its structure and GTPase activity investigated by using highly purified dynamin. *Mol. Biol. Cell* **3**, 1181–1194 (1992).
10. Takei, K., McPherson, P. S., Schmid, S. L. & De Camilli, P. Tubular membrane invaginations coated by dynamin rings are induced by GTP-gamma S in nerve terminals. *Nature* **374**, 186–190 (1995).
11. Ferguson, S. M. & De Camilli, P. Dynamin, a membrane-remodelling GTPase. *Nat. Rev. Mol. Cell Biol.* **13**, 75–88 (2012).
12. Thompson, H. M., Cao, H., Chen, J., Euteneuer, U. & McNiven, M. A. Dynamin 2 binds gamma-tubulin and participates in centrosome cohesion. *Nat. Cell Biol.* **6**, 335–342 (2004).
13. Tanabe, K. & Takei, K. Dynamic instability of microtubules requires dynamin 2 and is impaired in a Charcot-Marie-Tooth mutant. *J. Cell Biol.* **185**, 939–948 (2009).
14. Cao, H., Garcia, F. & McNiven, M. A. Differential distribution of dynamin isoforms in mammalian cells. *Mol. Biol. Cell* **9**, 2595–2609 (1998).
15. Herskovits, J. S., Burgess, C. C., Obar, R. A. & Vallee, R. B. Effects of mutant rat dynamin on endocytosis. *J. Cell Biol.* **122**, 565–578 (1993).
16. Kar, U. P., Dey, H. & Rahaman, A. Cardiolipin targets a dynamin-related protein to the nuclear membrane. *eLife* **10**, e64416 (2021).

17. Mannino, P. J. et al. Quantitative ultrastructural timeline of nuclear autophagy reveals a role for dynamin-like protein 1 at the nuclear envelope. *Nat. Cell Biol.* **27**, 464–476 (2025).

18. Papandreou, M. E., Konstantinidis, G. & Tavernarakis, N. Nucleophagy delays aging and preserves germline immortality. *Nat. Aging* **3**, 34–46 (2023).

19. Fonseca, T. B., Sánchez-Guerrero, Á, Milosevic, I. & Raimundo, N. Mitochondrial fission requires DRP1 but not dynamins. *Nature* **570**, E34–E42 (2019).

20. Park, R. J. et al. Dynamin triple knockout cells reveal off-target effects of commonly used dynamin inhibitors. *J. Cell Sci.* **126**, 5305–5312 (2013).

21. Janssen, A. F. J., Breusegem, S. Y. & Larrieu, D. Current methods and pipelines for image-based quantitation of nuclear shape and nuclear envelope abnormalities. *Cells* **11**, 347 (2022).

22. Goldman, R. D. et al. Accumulation of mutant lamin A causes progressive changes in nuclear architecture in Hutchinson-Gilford progeria syndrome. *Proc. Natl. Acad. Sci. USA* **101**, 8963–8968 (2004).

23. Scaffidi, P. & Misteli, T. Lamin A-dependent nuclear defects in human aging. *Science* **312**, 1059–1063 (2006).

24. Lattanzi, G. et al. Lamins are rapamycin targets that impact human longevity: a study in centenarians. *J. Cell Sci.* **127**, 147–157 (2014).

25. Matias, I. et al. Loss of lamin-B1 and defective nuclear morphology are hallmarks of astrocyte senescence in vitro and in the aging human hippocampus. *Aging Cell* **21**, e13521 (2022).

26. Ferreira-Marques, M. et al. Ghrelin delays premature aging in Hutchinson-Gilford progeria syndrome. *Aging Cell* **22**, e13983 (2023).

27. De Silva, N. S. et al. Nuclear envelope disruption triggers hallmarks of aging in lung alveolar macrophages. *Nat. Aging* **3**, 1251–1268 (2023).

28. Catarinella, G. et al. SerpinE1 drives a cell-autonomous pathogenic signaling in Hutchinson-Gilford progeria syndrome. *Cell Death Dis.* **13**, 737 (2022).

29. Sundborger, A. C. et al. A dynamin mutant defines a super-constricted prefission state. *Cell Rep.* **8**, 734–742 (2014).

30. Ramachandran, R. et al. The dynamin middle domain is critical for tetramerization and higher-order self-assembly. *EMBO J.* **26**, 559–566 (2007).

31. Macia, E. et al. Dynasore, a cell-permeable inhibitor of dynamin. *Dev. Cell* **10**, 839–850 (2006).

32. Ariotti, N. et al. Ultrastructural localisation of protein interactions using conditionally stable nanobodies. *PLoS Biol.* **16**, e2005473 (2018).

33. Schulze, R. J. et al. Lipid droplet breakdown requires dynamin 2 for vesiculation of autolysosomal tubules in hepatocytes. *J. Cell Biol.* **203**, 315–326 (2013).

34. Freund, A., Laberge, R. M., Demaria, M. & Campisi, J. Lamin B1 loss is a senescence-associated biomarker. *Mol. Biol. Cell* **23**, 2066–2075 (2012).

35. Kang, S. M. et al. Progerinin, an optimized progerin-lamin A binding inhibitor, ameliorates premature senescence phenotypes of Hutchinson-Gilford progeria syndrome. *Commun. Biol.* **4**, 5 (2021).

36. Berger, C. et al. Cryo-electron tomography on focused ion beam lamellae transforms structural cell biology. *Nat. Methods* **20**, 499–511 (2023).

37. Lascaux, P. et al. TEX264 drives selective autophagy of DNA lesions to promote DNA repair and cell survival. *Cell*, https://doi.org/10.1016/j.cell.2024.08.020 (2024).

38. Hagen, C. et al. Structural basis of vesicle formation at the inner nuclear membrane. *Cell* **163**, 1692–1701 (2015).

39. De Vos, W. H. et al. Repetitive disruptions of the nuclear envelope invoke temporary loss of cellular compartmentalization in laminopathies. *Hum. Mol. Genet.* **20**, 4175–4186 (2011).

40. Vargas, J. D., Hatch, E. M., Anderson, D. J. & Hetzer, M. W. Transient nuclear envelope rupturing during interphase in human cancer cells. *Nucleus* **3**, 88–100 (2012).

41. Karoutas, A. et al. The NSL complex maintains nuclear architecture stability via lamin A/C acetylation. *Nat. Cell Biol.* **21**, 1248–1260 (2019).

42. Gesson, K. et al. A-type lamins bind both hetero- and euchromatin, the latter being regulated by lamina-associated polypeptide 2 alpha. *Genome Res.* **26**, 462–473 (2016).

43. Rogakou, E. P., Pilch, D. R., Orr, A. H., Ivanova, V. S. & Bonner, W. M. DNA double-stranded breaks induce histone H2AX phosphorylation on serine 139. *J. Biol. Chem.* **273**, 5858–5868 (1998).

44. Wang, B., Matsuoka, S., Carpenter, P. & Elledge, S. 53BP1, a mediator of the DNA damage checkpoint. *Science* **298**, 1435–1438 (2002).

45. Singh, N. P., McCoy, M. T., Tice, R. R. & Schneider, E. L. A simple technique for quantitation of low levels of DNA damage in individual cells. *Exp. Cell Res.* **175**, 184–191 (1988).

46. Bakkenist, C. J. & Kastan, M. B. DNA damage activates ATM through intermolecular autophosphorylation and dimer dissociation. *Nature* **421**, 499–506 (2003).

47. Chen, X., Paudyal, S. C., Chin, R. I. & You, Z. PCNA promotes processive DNA end resection by Exo1. *Nucleic Acids Res.* **41**, 9325–9338 (2013).

48. Chernikova, S. B. et al. Dynamin impacts homology-directed repair and breast cancer response to chemotherapy. *J. Clin. Investig.* **128**, 5307–5321 (2018).

49. Bailly, C. Irinotecan: 25 years of cancer treatment. *Pharmacol. Res.* **148**, 104398 (2019).

50. Thomas, A. & Pommier, Y. Targeting topoisomerase I in the era of precision medicine. *Clin. Cancer Res.* **25**, 6581–6589 (2019).

51. Burute, M. & Kapitein, L. C. Cellular logistics: unraveling the interplay between microtubule organization and intracellular transport. *Annu. Rev. Cell Dev. Biol.* **35**, 29–54 (2019).

52. Lottersberger, F., Karssemeijer, R. A., Dimitrova, N. & de Lange, T. 53BP1 and the LINC complex promote microtubule-dependent DSB mobility and DNA repair. *Cell* **163**, 880–893 (2015).

53. Shokrollahi, M. et al. DNA double-strand break-capturing nuclear envelope tubules drive DNA repair. *Nat. Struct. Mol. Biol.* **31**, 1319–1330 (2024).

54. Vasquez, R. J., Howell, B., Yvon, A. M., Wadsworth, P. & Cassimeris, L. Nanomolar concentrations of nocodazole alter microtubule dynamic instability in vivo and in vitro. *Mol. Biol. Cell* **8**, 973–985 (1997).

55. Chen, J. G. & Horwitz, S. B. Differential mitotic responses to microtubule-stabilizing and -destabilizing drugs. *Cancer Res.* **62**, 1935–1938 (2002).

56. Wu, Y. et al. A dynamin 1-, dynamin 3- and clathrin-independent pathway of synaptic vesicle recycling mediated by bulk endocytosis. *Elife* **3**, e01621 (2014).

57. Lamm, N., Rogers, S. & Cesare, A. J. Chromatin mobility and relocation in DNA repair. *Trends Cell Biol.* **31**, 843–855 (2021).

58. Wang, Y. et al. Autophagy regulates chromatin ubiquitination in DNA damage response through elimination of SQSTM1/p62. *Mol. Cell* **63**, 34–48 (2016).

59. Qiang, L. et al. Autophagy positively regulates DNA damage recognition by nucleotide excision repair. *Autophagy* **12**, 357–368 (2016).

60. Dou, Z. et al. Autophagy mediates degradation of nuclear lamina. *Nature* **527**, 105–109 (2015).

61. Karantza-Wadsworth, V. et al. Autophagy mitigates metabolic stress and genome damage in mammary tumorigenesis. *Genes Dev.* **21**, 1621–1635 (2007).

62. Liu, E. Y. et al. Loss of autophagy causes a synthetic lethal deficiency in DNA repair. *Proc. Natl. Acad. Sci. USA* **112**, 773–778 (2015).

63. Mathew, R. et al. Autophagy suppresses tumor progression by limiting chromosomal instability. *Genes Dev.* **21**, 1367–1381 (2007).

64. Herve, S. et al. Chromosome mis-segregation triggers cell cycle arrest through a mechanosensitive nuclear envelope checkpoint. *Nat. Cell Biol.* **27**, 73–86 (2025).

65. Luithle, N. et al. Torsin ATPases influence chromatin interaction of the Torsin regulator LAP1. *eLife* **9**, e63614 (2020).

66. Nabbi, A. & Riabowol, K. Rapid isolation of nuclei from cells in vitro. *Cold Spring Harb. Protoc.* **2015**, 769–772 (2015).

67. Gowrisankaran, S. et al. Endophilin-A coordinates priming and fusion of neurosecretory vesicles via intersectin. *Nat. Commun.* **11**, 1266 (2020).

68. Aveleira, C. A. et al. Neuropeptide Y stimulates autophagy in hypothalamic neurons. *Proc. Natl. Acad. Sci. USA* **112**, E1642–E1651 (2015).

69. Gyori, B. M., Venkatachalam, G., Thiagarajan, P. S., Hsu, D. & Clement, M. V. OpenComet: an automated tool for comet assay image analysis. *Redox Biol.* **2**, 457–465 (2014).

70. Olive, P. L., Banáth, J. P. & Durand, R. E. Heterogeneity in radiation-induced DNA damage and repair in tumor and normal cells measured using the "comet" assay. *Radiat. Res.* **122**, 86–94 (1990).

71. Johnson, E., Seiradake, E. & Jones, E. Y. Correlative in-resin super-resolution and electron microscopy using standard fluorescent proteins. *Sci. Rep.* **5**, 9583 (2015).

72. Eisenstein, F. et al. Parallel cryo electron tomography on in situ lamellae. *Nat. Methods* **20**, 131–138 (2023).

73. Rohou, A. & Grigorieff, N. CTFFIND4: fast and accurate defocus estimation from electron micrographs. *J. Struct. Biol.* **192**, 216–221 (2015).

74. Zheng, S. et al. AreTomo: an integrated software package for automated marker-free, motion-corrected cryo-electron tomographic alignment and reconstruction. *J. Struct. Biol. X* **6**, 100068 (2022).

75. Buchholz, T.-O. et al. Content-aware image restoration for electron microscopy. in (eds Müller-Reichert, T. & Pigino, G.) *Methods in Cell Biology*, 277–289 (Academic Press, 2019).

76. Lamm, L. et al. MemBrain: a deep learning-aided pipeline for detection of membrane proteins in Cryo-electron tomograms. *Comput. Methods Prog. Biomed.* **224**, 106990 (2022).

77. Kremer, J. R., Mastronarde, D. N. & McIntosh, J. R. Computer visualization of three-dimensional image data using IMOD. *J. Struct. Biol.* **116**, 71–76 (1996).

78. Ermel, U. H., Arghittu, S. M. & Frangakis, A. S. ArtiaX: an electron tomography toolbox for the interactive handling of sub-tomograms in UCSF ChimeraX. *Protein Sci.* **31**, e4472 (2022).

79. Frangakis, A. S. It's noisy out there! A review of denoising techniques in cryo-electron tomography. *J. Struct. Biol.* **213**, 107804 (2021).

80. Pettersen, E. F. et al. UCSF ChimeraX: structure visualization for researchers, educators, and developers. *Protein Sci.* **30**, 70–82 (2021).

Acknowledgements

Author contributions

Conceptualization I.M. and C.A.; Experimentation C.A., T.M., L.C., R.G., F.W., N.R., and I.M.; Analysis C.A., T.M., L.C., M.L.C., I.My., J.B., N.R., and I.M.; Resources: I.M., N.R., K.R., P.L., A.C.R., and C.S.; Funding: N.R., K.R., and I.M.; Manuscript, figure preparation and revision: I.M., N.R., C.A., and T.M. (all coauthors contributed to the final manuscript).

Competing interests

The authors declare no competing interests.

Additional information